THE DESIGN OF FLUORESCENCE CORRELATION SPECTROSCOPY

FOR SINGLE MOLECULE TECHNIQUES

A Dissertation

presented to

the Faculty of the Graduate School at the University of Missouri-Columbia

In Partial Fulfillment
of the Requirements for the Degree
Doctor of Philosophy

by

Zenia Norman

Dr. Peter Cornish, Dissertation Supervisor

December 2019

The undersigned, appointed by the dean of the Graduate School, have examined the dissertation entitled

THE DESIGN OF FLUORESCENCE CORRELATION SPECTROSCOPY FOR SINGLE MOLECULE TECHNIQUES

presented by Zenia Norman,		
a candidate for the degree of doctor of philosophy,		
and hereby certify that, in their opinion, it is worthy of acceptance.		
	Dr. Peter Cornish	
	Dr. Shinghua Ding	
	211 Simighan 2 mg	
	Dr. Andrew Gu	
	Dr. Andrew Gu	
	Dr. Gavin King	

... To my family and those who have been there for me since day one

ACKNOWLEDGEMENTS

I would like to thank my advisor, Dr. Peter Cornish, for being a great mentor and friend throughout the years. I always enjoyed our conversations about research among our other talks about sports, life, and movies, etc. Thank you for being patient, especially when I thought I knew what I was doing...but later realized I was wrong. I really had enjoyed working with you (especially when it came to our electronic projects) and hope that we can continue our friendship for more years to come.

I would like to thank my committee Dr. Shinghua Ding, Dr. Andrew Gu, and Dr. Gavin King, for all the help they have provided.

Next, I would like to thank Dr. Tabbetha Dobbins for helping me with receiving this opportunity to attend the University of Missouri. I met Dr. Dobbins while attending Grambling State University. She was the one who introduced me to research, and it's has been history ever since.

I would like to thank my past labmates Dr. Bassem Shebl, Dr. Drew Menke, and Dr. Widler Casy, for all the great times we had together. Bassem, I always enjoy your thoughtfulness and our conversations. Drew, I really enjoyed the times we worked together with IGERT, and all the laughs we had. Casy, I always enjoyed our conversations and your positivity. You all have amazing stories and have become like brothers to me. I am happy to have experienced this journey with you all. To my other labmates, thank you for all the memories.

I would also like to thank Dr. Taub for helping me with this opportunity to make it to the University of Missouri as well.

Thank you to the friends that I was able to make throughout the last few years-Keisha, Janae, Rose, Cyd, and LaCassidy. I wish I could have met you all a little earlier in the journey, but it was better late than never.

To Antoinette Landor, whoever thought that we would have similar journeys of being from Louisiana, graduating from Grambling, and ending up at MU in different positions but at the same time. Thank you for being a close friend and a sister to me, for always keeping it real with me, and making these years bearable with all the laughs and conversations we had.

To Pamela Nunnelly, thank you for all the love and support throughout the years.

These 6 years that we have known each other seem like they have flown by a little too fast. Thank you for being on this journey with me, as well.

To my family, my mom, dad, sister, and brother, you had no idea what I was doing but were behind me all the way. Thank you for always being there for me when I needed you all. I know you all are all happy for me to complete this journey and are ready to see what is next.

To my close friends that have been with me since day one, thank you for all the motivation that you have given me throughout these years.

Finally, Quinn Jones, thank you for everything you have done for me. From making this big move to Missouri, to the laughs, and memories. It has truly been an adventure. Thank you for everything you have done throughout the years.

TABLE OF CONTENTS

	ACK	WON	/LEDGEMENTS	i
	LIST	OF I	FIGURES	. vi
	LIST	OF 7	TABLES	X
	ABST	RAG	CT	X i
1	Sin	gle N	Molecule Techniques to Study the Ribosome	1
	1.1	Intr	oduction	1
	1.2	Ove	erview of Protein Synthesis	3
	1.3	Wh	y Single Molecule Techniques?	5
	1.4	Sin	gle Molecule Techniques to Investigate Ribosome Dynamics	9
	1.4.	1	Dynamics of Initiator Factors and Ribosome Conformations	9
	1.4.	2	Investigation of Mutant Models Versus Wild Type	10
	1.4.	3	Dynamics of Ribosome Elongation	11
	1.4.	4	Translation Errors	11
	1.4.	5	Forces in Translation	12
	1.4.	6	Termination	13
	1.5	Sin	gle molecule studies of ribosome assembly	13
	1.6	Ain	a	14
2	Flu	oresc	ence Correlation Spectroscopy	15
	2.1	Intr	oduction	15
	2.2	The	eory of Diffusion	16
	2.3	Intr	oduction to Fluorescence	23
	2.4	Cor	nsiderations in Performing FCS Experiments	24
	2.4.	1	Dye Selection/Fluorophores	24
	2.4.	2	Sample Concentration	25
	2.5	Sign	nal to Noise by Time Scale	26
	2.5.	1	Nanosecond time scale (Region I)	27
	2.5.	2	Microsecond time scale (Region II- III)	27
	2.5.	3	Millisecond time scale (Region IV)	29
3	Sof	twar	e Design and Confocal Microscope Assembly	31

3.	1	Introduction	31
3.	2	Types of Correlators and Background of the Designs	33
	3.2.1	Multi Tau correlator	33
	3.2.2	Linear correlator	35
	3.2.3	Dual Correlator	36
3.	3	Dual FPGA Correlator Design	39
	3.3.1	FPGA	39
	3.3.2	Dual Correlator FPGA design	39
3.	4	FPGA Linear Design	41
	3.4.1	Target	41
	3.4.2	Host side	43
3.	5	Hardware Set-Up of Confocal Microscopy	46
	3.5.1	Excitation Pathway	49
	3.5.2	Emission Pathway	51
	3.5.3	Alignment of the Pinhole	51
4	Appl	lications and Verification	55
4.	1	Calibration	55
4.	2	Photobleaching	57
4.	3	Concentration Selection	58
4.	4	Correlator Test	58
	4.4.1	Rhodamine 6G Comparison	60
	4.4.2	TetraSpeck beads	62
4.	5	Acquisition Time	64
4.	6	Applications to Biological Molecules	67
	4.6.1	27 base m91 DNA	67
	4.6.2	Ribosome, mRNA, with labeled Alexa 546 DNA	68
4.	7	Summary	70
5	Outle	ook	71
5.	1	Corrections in the system	72
5.	2	Optimizations in the software	72
5.	3	Developments in the system	72
Refe	erence	es	74

T 7 T T T		
V / I' I · A	•	J'

LIST OF FIGURES

Figure 1-1 70S E Coli Ribosome. [1] The small subunit (30S) is shown in the blue/orange. The large subunit (50S) is shown in the red/green
Figure 1-2 The process of protein synthesis. The process begins with the joining of the two subunits with the help of initiation factors. Next, the elongation cycle begins by adding the amino acids delivered by the tRNA. The polypeptide chain grows until it encounters a stop codon. The termination process begins. Next, the ribosome is recycled, and the process of protein synthesis starts again.
Figure 1-3 Different single molecule techniques.
Figure 2-1 The PSF of the confocal volume
Figure 2-2 On the bottom left: larger molecules cause a shift to the right in the diffusion time. On the top right: the amplitude of the correlation curve decreases as the concentration increases.
Figure 2-3 Development of an autocorrelation curve.
Figure 2-4 The Jablonski diagram gives a visual description of the different energy levels that occur during the excitation of a fluorophore
Figure 2-5 The areas at which noise can affect the curve overtime. Region I – rotation and antibunching, Region II – inter-molecular processes, Region III- triplet formation, Region IV- diffusion
Figure 3-1 The sampling time doubles for each linear correlator 1, 2, and 3. In short, the multi tau correlator is a series of linear correlators at different sampling times. Linear correlator 1 is sampled at $1\mu s$, linear correlator 2 is sampled at $2\mu s$, and the correlator 3 is sampled at $4\mu s$, etc.
Figure 3-2 In the linear correlator, the sampling time remains constant. Therefore, if a correlator has a sampling time of $1\mu s$ and the user would like to calculate up to 1 second. It would take 10^6 data points to calculate the correlation curve
Figure 3-3 Top: the design of the linear correlator. Bottom: The design of the multi tau correlator. The design of the dual correlator is the linear correlator combined with the multi tau correlator. The two correlators are run simultaneously
Figure 3-4 NI 9402 C module receives the signal from the detector
Figure 3-5 Flow of FPGA Linear Correlator
Figure 3-6 Screenshot of the Dual correlator and the multi tau correlator. The dual correlator gives a smoother look to the curve because of the larger bins set to microseconds, while the multi tau correlator is sampled at 50 ns and is noisier because of the smaller bins. The yellow data points on the dual correlator represent information from the linear correlator, while the green data points are from the multi tau correlator 45

Figure 3-7 Layout of the FCS system.	. 47
Figure 3-8 Layout of the system. The image shows the full layout of the FCS system. To black box contains the emission pathway. The box is used to eliminate light that could interfere with the emission pathway.	
Figure 3-9 The image shows the alignment of the excitation pathway	. 49
Figure 3-10 Image shows the placement of the objective lens, which is crucial for creating the confocal spot.	. 50
Figure 3-11 The pinhole helps create the confocal volume by eliminating out of focus light from the focal point. The emission light passes through the pinhole and is then collimated with the 200 mm lens (L3). Collimation of the light helps keep the beam frod diverging. The Raman filter eliminates the Raman signal from the signal. The filter can have some effect in eliminating the necessary signal since the emission light and the Raman light overlaps.	1
Figure 3-12 Emission pathway of the setup. The light is directed onto APD 1 and APD using a dichroic mirror. In the FCCS setup, the dichroic mirror will separate the two signals.	
Figure 3-13 The APD detector	. 54
Figure 3-14 The NI 9481 is a relay that switches the APDs on and off	. 54
Figure 4-1 The nonlinear trend in our count rate is shown. We conclude that the trend i due to the afterpulsing of the APD detector. This afterpulsing will be corrected in the future.	
Figure 4-2 Photobleaching of the dye was observed in experiments that used coverslips. This is due to the sample being restricted to a small surface area. The samples that were made with slides, bleached less, and were more stable.	e
Figure 4-3 Information about figure legend	. 59
Figure 4-4 RG6 dye on the dual correlator. Residuals show that the data fits better compared to the multi tau correlator. The first data point is an indication of detectors afterpulsing.	. 60
Figure 4-5 The multi tau correlator results show that the data is noisier compared to the dual correlator but gets smoother in the millisecond range. Spikes could occur from Poisson noise or aggregation of the dye.	
Figure 4-6 Dual Correlator with TetraSpeck beads	. 62
Figure 4-7 Multi tau correlator with TetraSpeck beads. Results are like the dual correlator.	. 63
Figure 4-8 5 second measurements	. 65
Figure 4-9 10 second measurements	65

Figure 4-10 30 second measurement	66
Figure 4-11 60 second measurement	66
Figure 4-12 Dual correlator results from the DNA	67
Figure 4-13 Multi tau correlator results of the DNA.	68
Figure 4-14 Quick Fit results of the labeled DNA, mRNA, and ribosome sample. Two components were able to be fit from our curve.	69

LIST OF TABLES

Table 1-1 Brief summary of Single Molecule Instruments
Table 2-1 Fitting models [73]
Table 3-1 A list of available software correlators and the samples that were used to verify the systems.
Table 3-2 FPGA terms
Table 3-3 List of Parts for the FCS Set-up
Table 4-1 Comparison of the count rate to the concentration
Table 4-2 The laser power was compared to the intensity values. CPS highlighted in orange represent count rates that caused software overflows for the dual correlator. 100 nM was determined to be a good concentration to start calibrations
Table 4-3 Orange box represents the outlier in the data. The table shows how $x2$ values get better as the measurement time increases. Indicating that the SNR gets better over
time

ABSTRACT

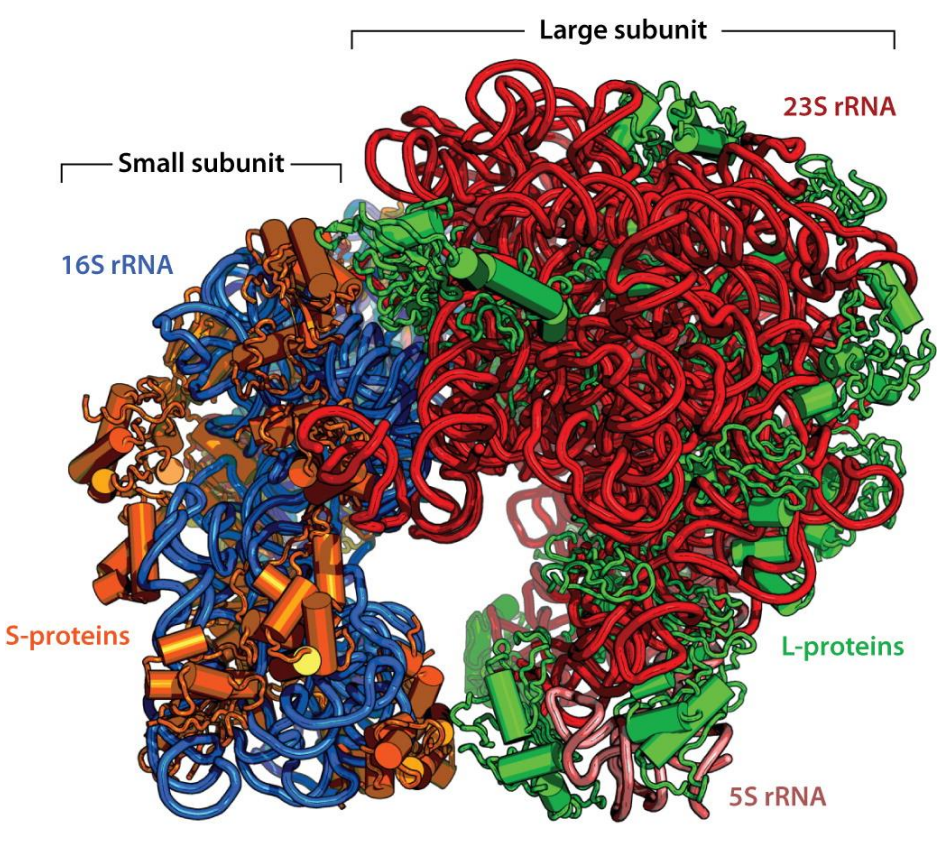
The ribosome is responsible for protein synthesis- a critical process in creating essential proteins for cell survival. Though bulk techniques yield valuable results about the structure of the ribosome, bulk techniques are not ideal in examining ribosomal dynamics and understanding kinetics involved in protein synthesis. On the contrary, the single molecule spectroscopy techniques are ideal in investigating the mechanisms of ribosome dynamics in real-time under equilibrium conditions. The latest advances in single molecule biophysics have opened numerous opportunities in the biological world to study the dynamics of molecules in real-time. Single molecule techniques such as Fluorescence Correlation Spectroscopy (FCS) have opened opportunities to study the ribosome as well as other ribosomal proteins. FCS is used to investigate diffusion coefficients, concentration, and kinetics of biological samples. In this thesis, we address the process of assembling an FCS system, as well as the design of a high-speed correlator. The high-speed correlator allows the software to handle the high data counts that can occur in single molecule experiments. A field-programmable gate arrays (FPGA) dual correlator and a multi-tau correlator are designed to handle the noise and high count rates that can dominate the signal. Also addressed in this thesis are ideal experimental conditions for successfully obtaining and troubleshooting results received from FCS curves.

1 Single Molecule Techniques to Study the Ribosome

1.1 Introduction

Protein synthesis is the process of making proteins for the body- an essential factor in producing proteins is the ribosome. The 70S E Coli ribosome (figure 1-1) acts as a large molecular machine- using external GTP hydrolysis to create proteins that are essential components of cell survival. The ribosome consists of two subunits- the small subunit, 30S, and the large subunit, 50S. The ribosome is composed of proteins, as well as ribosomal RNA. The small subunit contains 21 ribosomal proteins (labeled S1-S21), and a 16S ribosomal ribonucleic acid (rRNA) strand where S1-S21 assemble. The small

subunit divides into the body (5' domain), the platform region (central), and the head (3' domain). The large subunit contains 33 proteins (labeled L1-L36) and two rRNAs strands- the 23S and the 5S. Explained in detail later, the small subunit and the large subunit assemble to provide a platform for transfer RNAs (tRNAs) and messenger RNAs (mRNAs) to assemble or bind together.



Rannu. Rev. Biochem. 80:501–26

Figure 1-1 70S E Coli Ribosome. [1] The small subunit (30S) is shown in the blue/orange. The large subunit (50S) is shown in the red/green.

Annual review of biochemistry by ANNUAL REVIEWS. Reproduced with permission of ANNUAL REVIEWS in the format Thesis/Dissertation via Copyright Clearance Center.

Protein synthesis can be broken down into three steps: initiation, elongation, and termination. In keeping, ribosome dynamics are key in protein synthesis. As demonstrated later, several studies have revealed the importance of understanding ribosomal dynamics, as each factor plays a role in ensuring that protein synthesis performs correctly. Errors in translation can be linked to diseases such as HIV. Therefore, the ribosome is seen as a therapeutic target. Antibodies have been designed to target the ribosome dynamics- causing it to lock into specific subunit conformations. [2, 3, 4]

During protein synthesis, the ribosome interacts with mRNA, tRNA, and other non-ribosomal cofactors to assure correct initiation, elongation, and termination of polypeptide chains.

1.2 Overview of Protein Synthesis

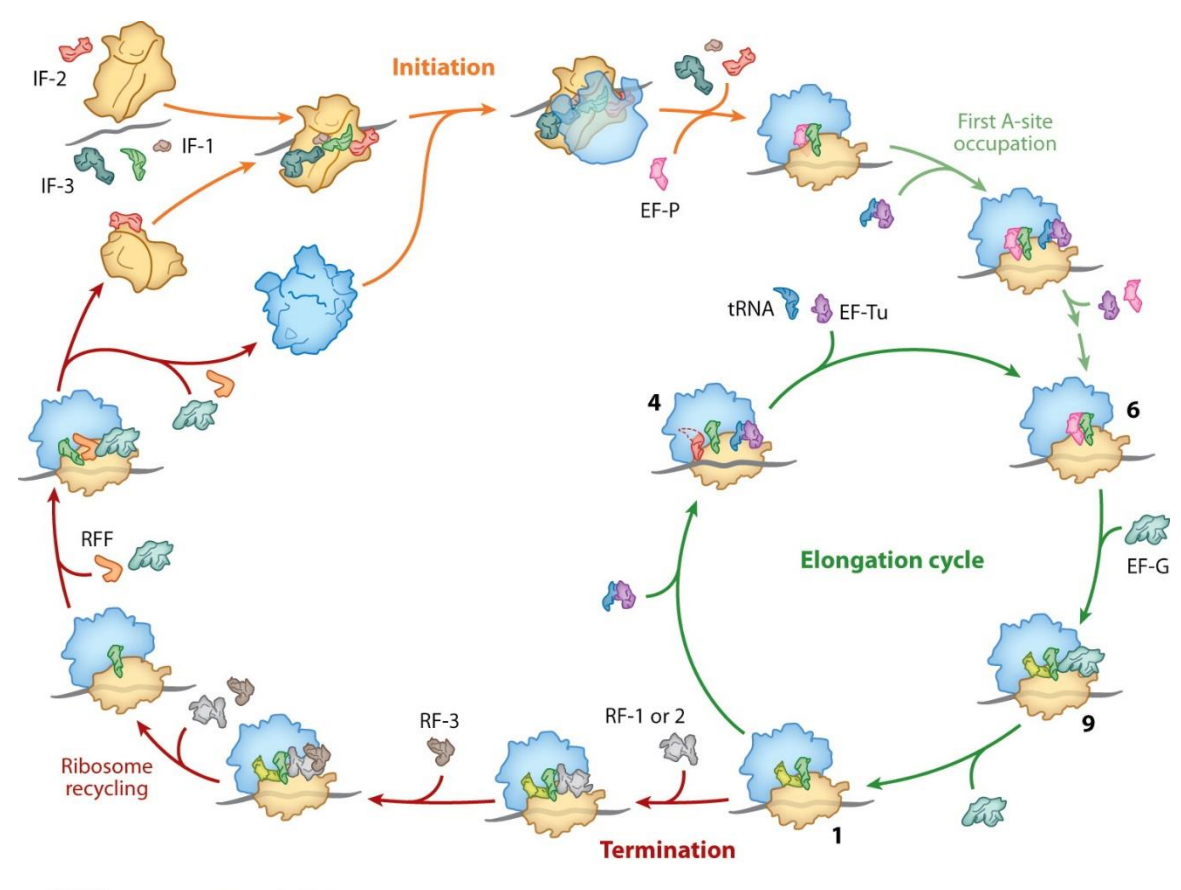
The ribosome contains three sites; the A-site, where the tRNA transports in the amino acid, the P-site, where the peptidyl tRNA forms, and the E-site, where the tRNA exits. The small subunit facilitates base-pairing – the translation of the genetic information delivered by mRNA. In accordance, the large subunit hosts the catalytic peptidyl transferase center (PTC), which is responsible for peptide bonding. Each tRNA collects the proper amino acids from the cytoplasm with the help of initiator factors and delivers them to the ribosome to begin protein synthesis.

At each step, the mRNA translocates through the ribosome reading nucleotides from the start codon (initiating codon) to stop codon (termination codon)- along the length of the open reading frame. Proteins known as initiation factors, IF1, IF2, and IF3, help guide and regulate the initiation step of protein synthesis- allowing for correct positioning of the reading frame. IF2 and initiator tRNA facilitates small subunit binding

to the large subunit. IF1 and IF3 allow for correct positioning of the reading frame- to the 5'-AUG-3' of the mRNA (AUG), forming a small subunit preinitiation complex (PIC). Base pairing between the mRNA-Shine Dalgarno (SD) and the small subunit anti-SD allow for the stabilization of the small PIC. [5, 6]

After GTP hydrolysis on IF2- IF2 dissociates from the ribosome complex and the ribosome begins the process of elongation. Elongation involves an iterative cycle of adding amino acids delivered by tRNA into a growing polypeptide chain. Just like the initiation process, elongation factors, EF-Tu and EF-G, help facilitate the elongation process. Each elongation cycle starts with a nascent polypeptide chain occupied in the P site. E-Tu loads the aminoacyl tRNA that carries the next amino acid into the A site of the ribosome. Next, tRNAs translocate from the A to P sites and from the P to E sitescarrying the mRNA along. [7]

As the peptide chain moves into the A/P site, ribosome dynamics come into action as the ribosome rotates spontaneously between the classical and hybrid states. The deacylated E-site tRNA leaves the ribosome, and the ribosome returns to the classical state. Next, EF-G-GDP leaves the ribosome, and the ribosome is ready for the next elongation cycle. The ribosome encounters a stop codon in the A site initiating the start of the termination step. Upon the binding of the release factors (RF), RF1 or RF2, the nascent polypeptide chain is disassembled from the ribosome complex. Hydrolysis of the nascent polypeptide deacetylates peptidyl-tRNA that is in the P site. Ribosome recycling factor (RRF) recognizes the post-termination ribosome complex and disassociates the small and large ribosomal subunits. [8]



Moore PB. 2012. Annu. Rev. Biophys. 41:1–19

Figure 1-2 The process of protein synthesis. The process begins with the joining of the two subunits with the help of initiation factors. Next, the elongation cycle begins by adding the amino acids delivered by the tRNA. The polypeptide chain grows until it encounters a stop codon. The termination process begins. Next, the ribosome is recycled, and the process of protein synthesis starts again.

Annual review of biophysics by Annual Reviews. Reproduced with permission of Annual Reviews in the format Thesis/Dissertation via Copyright Clearance Center. [9]

1.3 Why Single Molecule Techniques?

The ribosome is studied at either the bulk level or the single molecule level. In 1995, Joachim Frank and Hogler Starks produced the first three-dimensional images of the ribosome using cryo-electron microscopy (EM) [9]. Later, Cryo-EM studies revealed the first conformational states of the ribosome, suggesting that the ribosome moved in a

ratchet-like state- this declaration was later confirmed by smFRET. [5, 10, 11] Around the year 2000, X-Ray diffraction revealed high-resolution structures of the 70S ribosome. [12]

However, bulk techniques are not ideal in studying dynamics as movement can appear as a blur in the data collected, and the averaged information may mask out dynamic information. Single molecule methods have opened new opportunities for studying biological samples by achieving high sensitivity and high resolution while providing insight into the behavior of the individual molecules. [13]

With the optimization of instrumentation, single molecule detection has increased in sensitivity – allowing for the ability to detect 1.66×10^{24} mole of the sample. [14] This sensitivity has allowed researchers to overcome the disadvantages of ensemble averaging found in bulk techniques. Single molecule techniques provide a way of looking at systems under equilibrium conditions without the need for synchronization. Therefore, there has been an increased interest in using single molecule techniques- as single molecule techniques overcome shortcomings of the bulk technique and can serve as an approach to confirm bulk methods.

On the contrary, shortcomings in single molecule detections are the limits of photostability of fluorescent molecules, i.e., bleaching of dyes. [15] Also, poor statistics can be a disadvantage as countrates from experiments are low. Therefore, instrumentation resolution and signal to noise is essential to obtain results. [12, 16, 15] Several single molecule techniques exist in studying ribosome dynamics. Fluorescence- and force-based tools are the two major branches of single molecule techniques. These techniques can be used to investigate dynamic and immobilized samples. [15, 14]

SINGLE MOLECULE INSTRUMENTS

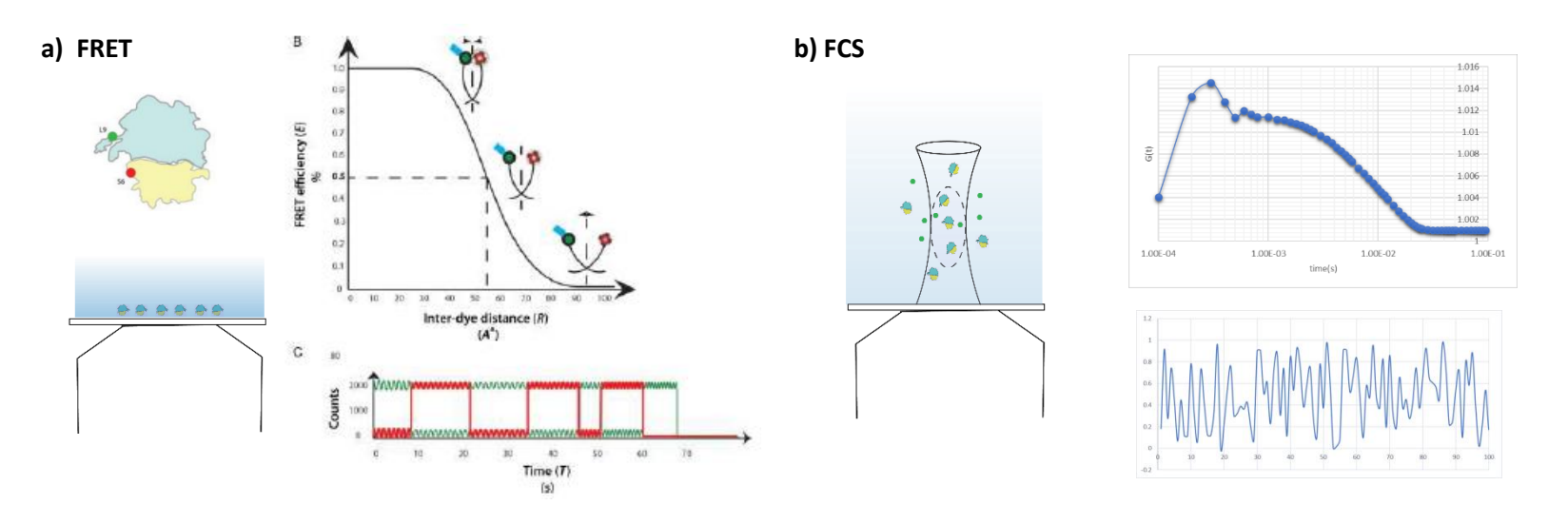
Immobilized Studies. Single molecule Forster resonance energy transfer (smFRET) is a distance-dependent fluorescence technique that uses surface immobilization of fluorescently tagged ribosomal proteins pairs to study distance-dependent dipolar interactions between the excited state of two dyes. TIRF (total internal reflection fluorescence) can be combined with FRET to help eliminate background noise. In biological applications, one molecule is represented as a donor, while the other molecule is the acceptor. The donor molecule is excited by a laser, and if the emission spectrum of the donor molecule overlaps the absorption spectrum of the acceptor molecule, then the energy is transferred to the acceptor molecule – releasing a photon. A FRET set-up is depicted in figure 1-3. Fluctuations in intensities from FRET measurements are detected by charge-coupled devices (CCD cameras). The images are taken from the CCD camera, and FRET histograms are built. The histograms are fit to a Gaussian distribution that yields conformational states, kinetic data, and lifetime distributions. [17]

Force – Based Studies. Optical tweezers are a force base single molecule technique that is used to determine mechanical forces. Using optical tweezers, researchers can study the mechanistic folding and unfolding of molecules by applying a mechanical force. Laser light is tightly focused through a lens, allowing an object to become trapped in a microfluid sample chamber, where forces are applied to a bead. Scattering components of the force pushes a silicone bead that is attached to the end of a molecule. An electric stage is used to move the trap, causing the molecule to stretch under a known displacement. With the knowledge of the trap stiffness (measured through traditional calibrations, i.e., equipartition theorem) and the displacement, researchers can use Hooke's law to measure the mechanical force. Various optical tweezers exist: single trap optical tweezers use a suction pipette and an optical trap at the other end; high-resolution dual trap uses optical traps; dual trap/fluorescence hybrid uses a dual trap design with a fluorescently labeled immobilized sample [18, 12]

Diffusion Studies. Fluorescence Correlation Spectroscopy (FCS) is a diffusion-based pseudo single molecule technique that correlates the time that molecules diffuse through a confocal spot. It is known for single molecule detection and is frequently built with a confocal microscope setup. Home built FCS systems use the software, i.e., LabVIEW, to count fluctuations detected from fluorescently labeled proteins using avalanche photodiodes (APD). These fluctuations are correlated, and information such as binding activities, diffusion coefficients, and concentration can be determined through the analysis of the data. FCS is typically used to investigate binding molecules.

Table 1-1 Brief summary of Single Molecule Instruments

SINGLE MOLECULE TECHNIQUES



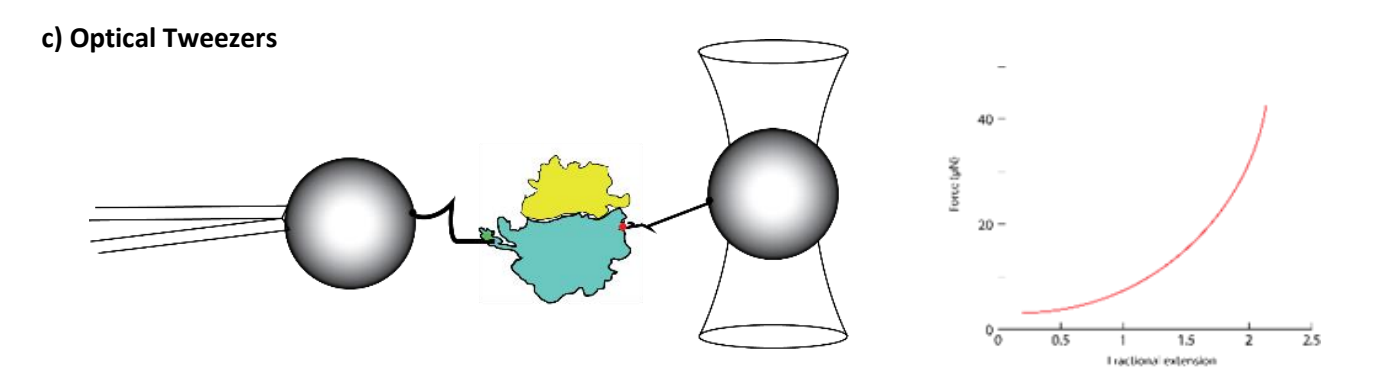


Figure 1-3 Different single molecule techniques.

 ∞

1.4 Single Molecule Techniques to Investigate Ribosome Dynamics

1.4.1 Dynamics of Initiator Factors and Ribosome Conformations

Researchers have studied the role of initiator factors using optical tweezers and smFRET to investigate how each initiator factor contributes to the start of protein synthesis. To begin with, the presence of IF2 and IF3 promotes subunit joining. Rupture forces between small complexes were investigated using optical tweezers to gain an understanding of the order of binding of initiation factors. Once the mRNA binds to the small subunit through anti-codon – codon pairing, it is then dislocated during initiation at a weak force of 5.7 pN. Next, IF2 binds to the ribosome and recruits initiator tRNA, where a more significant force of 16.1 pN is measured to dislocate mRNA.

This increase in force was linked to the codon-anticodon interactions that are found in the P site of the ribosome. The IF2/initiator tRNA complex then binds to the large subunit increasing the rupture force by 5 pN resulting in the stability of the 70S initiation complex. Stability of the mRNA is required for the successful pairing of tRNA anticodon and the mRNA codon. It was determined that the large subunit and IF2 plays a significant role in stabilizing the mRNA-ribosome interaction. [19]

Furthermore, the effect of the stability of IF2 was monitored in the presence of IF1 and IF3. Wang varied the IF2 in the presence of IF1, IF3, and combined IF1/IF3. Labeled IF2-tRNA and various tRNAs were observed in different FRET states, showing that the dynamics changed in the presence of each varying factor. In continuing, dynamics were investigated in varying combinations of IF, 30 ICs, and codons. IF2 was

found to significantly destabilize in the presence of IF3, while it remained stabilized in the absence of IF3. [20]

To understand more about the mechanism of subunit joining, Ling et al. used smFRET to monitor the dynamics of the L1 stalk of the large subunit during subunit association. Upon subunit joining- indicated by a 0.5 FRET state- the ribosome adopted a semirotated conformation, while the L1 stalk remains in a half-closed state. The presence of aa-tRNA, fMet-tRNA-fMet, and GTP bound IF2 shifted the ribosome into a semirotated state. Also, subunit rotation was observed in the presence of GTP-shifting the ribosome into a nonrotated confirmation. [21]

IF2 is known to facilitate subunit joining in the presence of GTP, while IF1 and IF3 help ensure that the ribosome bind correctly- serving as a proofreading tool. Elvekrog et al. observed the dynamics of initiator factors in the presence of IF3 and small initiation complex (IC) with competitions of IF1, IF2, or IF1/IF2. Three conformation states were observed in the presence of a completed 30IC complex. In continuing, significant subunit rotation was observed in the presence of different codons and tRNA. Thus, a stabilized conformation of IF3 indicated a correctly assembled small IC. [22] This study exhibited how IF3 is necessary in the correct formation of the 70S IC. Observed transitions between the zero FRET state and non-zero FRET state indicated a large subunit and small IC binding. [23] After IF3 binding, IF2 facilitates subunit joining by speeding up the rate of the process.

1.4.2 Investigation of Mutant Models Versus Wild Type

Investigation of the domain characteristics of labeled wild type IF2-GTP and labeled mutant (MT) IF2 were made in the presence of 30 IC and 30 IC MT, respectively. The

dwell times of the mutant models moved slowly between zero FRET and nonzero FRET, indicating that mutant models had a higher affinity compared to wild type. GTP was substituted for GDP and observed in the presence of the previous model. IF2 (GDP) bound complexes were more transient than the IF2 (GTP) complexes showing a ~30 fold larger Kd value. A major finding is that the conformations of domain III of IF2 domain I-domain III were found to contribute to the affinity of IF2(GTP) for the small IC. This result indicates that the specific domains of IF2 can be targeted for antibiotic treatment.

1.4.3 Dynamics of Ribosome Elongation

Cornish studied ribosome intersubunit rotation during elongation-fluorescently labeled proteins S6 and L9 were observed using smFRET. A high FRET state corresponded to the non-rotated conformation of the ribosome, while the low FRET state corresponded to the rotated state of the ribosome- where the tRNA occupies the A/P and P/E states of the ribosome. [25] The ribosome was found to rotate from a classical state to a hybrid state in a ratchet-like motion, as the mRNA translocated throughout the ribosome. Moreover, the binding of EF-G was revealed to shift the conformation of the ribosome into the rotated state. [26] Additionally, a number of experiments investigated the ribosome dynamics in the presence of EF-G, GTP hydrolysis, and other structural dynamics using smFRET. [27, 28, 29, 30, 31, 32, 33, 34, 35, 36]

1.4.4 Translation Errors

Problems can occur during translation, such as frameshifting – a mechanism that can stall and shift the ribosome backward in the presence of structured mRNA. To investigate

frameshifting, fluorescently labeled E. Coli. proteins S6 and L9 were assembled on a short mRNA attached to structured RNA (dnaX hairpin) outside of the mRNA entrance of the ribosome. The dnaX hairpin was used as a "roadblock" to stall the ribosome during normal translation. smFRET results revealed a new conformational state in the presence of the hairpin with a FRET value of (~0.22), known as the hyper-rotated state. The hyper-rotated state was discovered to rotate further than the distance estimated in the hybrid conformational state. This lower FRET state was observed in the presence of structured mRNA and, therefore, was not present in previous Cornish results during normal translation. [3] In some cases, the ribosome can even bypass or hop over sections of the mRNA during translation - scanning the mRNA for a landing codon before resuming translation [37].

1.4.5 Forces in Translation

Forces occurring during elongation and protein folding provide evidence that the ribosome reads three nucleotides at a time. [38, 39, 40] Studies reveal that ribosomes translate in a series of pause cycles. Pause times observed in the data related to the ribosome reading one codon at a time, and the unwinding of RNA. [41] Liu et al. observed how much force occurred during translocation. The forces were applied to the 3'end of the mRNA and the small subunit (S16) using optical tweezers. The ribosome generates $\sim 13 \pm 2$ pN of force- a force which is insufficient to unwind structured mRNA. In continuing, the ribosome jumps directly from one codon to the next during the mRNA translocation and does not move in smaller steps. Liu found that the stall forces correlated well with the amount of force to unwind structured mRNA; thus, the magnitude of both the RNA and stall force affects the rate of translation. [42]

1.4.6 Termination

Dynamics of the ribosome were investigated using smFRET in the presence of ribosome release factors R1, R2, and R3. Sternberg et al. used smFRET to demonstrate how RFs move dynamically throughout the termination process. Fluorescently labeled FRET pairs L1 ribosomes and tRNA were investigated to understand if tRNA induces dynamics in the A-site. A low FRET value of (0.2) determined that the tRNA did not induce a dynamic state during the deacylation of the peptidyl-tRNA. A high FRET value of (~.95) between RF1: tRNA indicates that the RF1 binds stably in the A site. A high FRET state of (~0.8)-indicated that RF3 stabilized the ribosome during the release of the RF1.

Sternberg determined that dynamics during termination is an organized system, which rotates into different conformational states such as the classical and hybrid states during the elongation cycle. [8] Studies conclude how R1/R3/TP complexes assemble to the ribosome to promote the process of termination. [43]

In keeping, other recycling factors, such as YaeJ, were investigated to determine its' role in ribosome recycling. YaeJ was found to stabilize the ribosome in the nonrotated state. [44] Conformational dynamics were monitored in the presence and absence of RRF- revealing that the ribosome rotated similar to the dynamics of elongation during termination. [45]

1.5 Single molecule studies of ribosome assembly

Ribosome biogenesis is the process of how the ribosome assembles. Nomura and Nierhaus studies yielded the first assembly maps of the small and large ribosome subunits, respectively. [46] At the time, it was thought that the ribosome binds in a

hierarchical order- where proteins bind in a specific order, and one protein cannot bind without the other preceding it. [47, 48, 49, 50, 51, 52].

Recently, Ridgeway used Fluorescence Triple-Correlation Spectroscopy (F3CS) – an expanded version of FCS-to study ten small intermediate ribosomal proteins in assembly. F3CS is compatible in investigating multiple proteins and is therefore ideal in studying multiple binding events during assembly. Ridgeway studied the assembly of the head domain of the small subunit by partial reconstitution of the 16S rRNA and six proteins (S7, S9, S10, S13, S14, S19). Low diffusion times observed through measurements indicated that the proteins bind to each other. Ridgeway discovered that the ribosome assembly did not bind in a hierarchical order, which contradicted with Nomura maps. However, it is considered that the Nomura maps were accurate in predicting the final position of the ribosomal proteins post assembly. [53]

1.6 Aim

In continuing, we would like to build on the theory of studying the ribosome using FCS, as it has opened new opportunities for exploring different avenues of dynamics.

Therefore, the aim of this thesis is to design a confocal FCS system and high-speed FPGA software correlator to investigate ribosome dynamics. Chapter 2 provides a discussion of the fundamental theory of fluorescence and FCS. Chapters 3 gives a step by step description of how to build the microscope system and information about the design of our FPGA dual correlator software. Chapter 4 gives information about the validation of the system. Chapter 5 provides an outlook and further discussion about future projects.

2 Fluorescence Correlation Spectroscopy

2.1 Introduction

Fluorescence correlation spectroscopy (FCS) is a robust single molecule technique that is used to investigate diffusion coefficients, concentration, and kinetics of biological samples. FCS was established in 1974 [54, 55] and was used to examine the diffusion and the unwinding of DNA. [47, 48, 49] FCS first suffered from low signal-to-noise ratios (SNR) and low sensitivity, leading to experiments requiring high concentrations of the sample- which was not ideal for biological studies. Impurities from higher concentrations contributed significantly to the background noise.

Twenty years later, Rigler improved the technique by combining FCS with a confocal microscope setup, therefore, enhancing the sensitivity of FCS by reducing the

noise that typically overwhelmed correlation results. [56, 57] The adaptation of the confocal setup allowed for a femtoliter observation volume, known as the detection volume- turning FCS into a single molecule technique. FCS was developed on the theory of diffusion and the theory of dynamic light scattering. [56, 58, 59, 60]

2.2 Theory of Diffusion

Diffusion is the process by which particles move from areas of high concentrations to areas of low concentrations. On the macroscopic level, Fick's first and second laws describe the rate of the diffusion of a solute across an area. Fick's first law gives a mathematical explanation of how diffusion works:

$$J_x = -D\frac{\partial C}{\partial x} \tag{2.1}$$

where C is the concentration, x is the position, D is the diffusion coefficient, and J_x is the diffusion flux. Fick's second law examines the rate of fluctuations in the concentration as they diffuse in and out of the specific volume with respect to time. The concentration C in a volume element fluctuates as a result of molecules diffusing in and out of the volume:

$$\frac{\partial C(\vec{r},t)}{\partial t} = D\nabla^2 C(\vec{r},t), \quad \text{where } \nabla^2 = \frac{\partial^2}{\partial x^2} + \frac{\partial^2}{\partial y^2} + \frac{\partial^2}{\partial z^2}$$
 (2.2)

where $C(\vec{r},t)$ is the concentration, and D is the diffusion coefficient of the molecule.

The focal volume is defined as a spatial function $\phi(\vec{r})$ that exists in the excitation volume, which leads to fluctuations in the concentration of a species. Molecules can travel throughout the confocal volume without changes in concentration. Ignoring any contributions from photophysical properties, detection electronics, etc., the concentrations of the fluorophores in the excitation volume at any point in time is:

$$\delta F(\vec{r},t) = \int \phi(\vec{r}) \delta C(\vec{r},t) d^3r \qquad (2.3)$$

where $\delta C(\vec{r},t)$ and represents the concentration fluctuations at location \vec{r} and time t, and $\phi(r)$ presents the point spread function (PSF). The molecules diffuse through the shape of the confocal volume:

$$PSF(x, y, z) = I_0 exp \left[-2 \left(\frac{x^2 + y^2}{\omega_{xy}^2} \right) + \frac{z^2}{\omega_z^2} \right]$$
 (2.4)

 ω_{xy} , ω_z is the transverse and axial waist. The size of the effective focal volume, V_{eff} , is defined as

$$V_{eff} = \pi^{3/2} \cdot \omega^2_{xy} \cdot z_0 \tag{2.5}$$

where ω_{xy} is the width in the xy-plane and z_0 is the z-direction of the confocal focus.

[61]

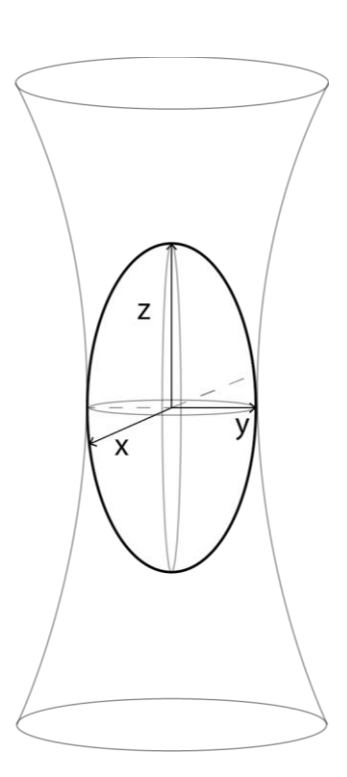


Figure 2-1 The PSF of the confocal volume.

On the microscopic level, Einstein considered the collective motion of Brownian motion by studying the impact of pollen particles in water as it travels in a given time. Einstein was able to determine that Brownian motion causes a random walk due to the particles colliding. Brownian motion leads to diffusion, which is the net movement of particles away from where it started. The displacement of the particles is proportionally related to the diffusion coefficient:

Diffusion in 1-D
$$\langle \Delta x^2 \rangle = 2Dt$$
 (2.6)

Diffusion in 2-D
$$\langle \Delta x^2 \rangle + \langle \Delta y^2 \rangle = 4Dt$$
 (2.7)

Diffusion in 3-D
$$\langle \Delta x^2 \rangle + \langle \Delta y^2 \rangle + \langle \Delta z^2 \rangle = 6Dt$$
 (2.8)

where D is the diffusion coefficient and Δx , Δy , Δz are the displacements in one -, two-, and three-dimension, respectively. The diffusion coefficient (units = $\mu m^2 \cdot s^{-1}$) describes the speed of which the particle diffuses through a volume.

Larger particles are more likely to collide into each other, causing the particle to diffuse more slowly- while the smaller particles are more mobile- allowing for faster diffusion. In short, the speed of diffusion is affected by the size or molecular mass of the particle in question. The Stokes-Einstein- equation relates the diffusion to the physical, measurable quantity of a molecule,

$$D = \frac{k_B T}{6\pi \eta r} \tag{2.9}$$

where k_B is the Boltzmann's constant (1.3806504 · 10^{-23} J/K), T is the absolute temperature, r is the hydrodynamic radius of the diffusing molecules, and η is the viscosity of the medium.

If the size of the volume and the diffusion coefficient is known, then the time it takes an object to diffuse through a volume, i.e., a cell can be calculated using the equation below:

$$\tau_D = \frac{\omega^2_{xy}}{4D} \tag{2.10}$$

where D is the diffusion coefficient, ω is the width or size of the volume and τ_D is the diffusion time.

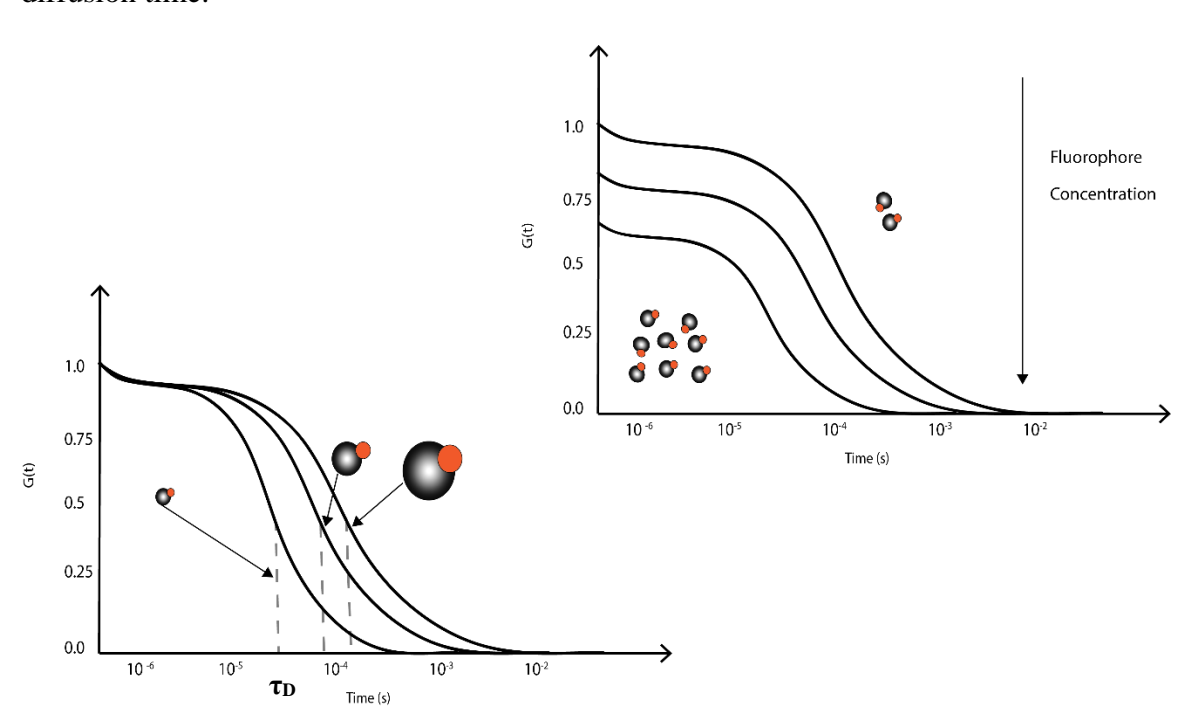


Figure 2-2 On the bottom left: larger molecules cause a shift to the right in the diffusion time. On the top right: the amplitude of the correlation curve decreases as the concentration increases.

The probability of randomly detecting a fluorophore in a confocal volume is based on Poisson distribution.

$$P(n,N) = \frac{\langle N \rangle^n e^{-\langle N \rangle}}{n!} \tag{2.11}$$

P(n, N) is the probability of n fluorophores being present in the confocal volume.

Fluctuations in intensity occur as molecules diffuse in and out of the volume. The number

of fluorophores and intensity will change based on the speed of the diffusion. Therefore, if the diffusion is fast, the change in the occupation number and intensity of the fluorophores will increase - if the diffusion is slow, the fluorophores will move slowly out of the volume, and the intensity will decrease (figure 2-2). [62]

The number of molecules in the focal volume and the concentration (C) are inversely related to the correlation amplitude (G),

$$G(0) = \frac{1}{N} = \frac{1}{V_{eff}C} \tag{2.12}$$

where N is the number of molecules and V_{eff} is the detection volume.

As molecules diffuse in and out the confocal volume, tiny fluctuations occur due to the excited molecules in the confocal volume. These fluctuations are compared with themselves, providing an analysis of the self-similarity of the intensity signal (figure 2-3). The fluctuations are analyzed using the correlation of the fluorescence intensity:

$$G(\tau) = \frac{\langle \delta F(t) \delta F(t+\tau) \rangle}{\langle F(t) \rangle^2}$$
 (2.13)

where G is the autocorrelation function, F(t) is the fluorescence intensity at time t, and τ is the lag time. The intensity at time F(t) is compared with the intensity at time $F(t + \tau)$. The autocorrelation is given by the product of the intensity times over the measurement time T. The fluctuations around the time average represent the number of molecules in the volume.

$$\delta F(t) = F(t) - \langle F(t) \rangle$$
 (2.14)

is the function of fluctuations around the mean for F(t).

The curves are fit to the Gaussian fit function:

$$G(\tau) = \frac{1}{N} \left(1 + \frac{\tau}{\tau_D} \right)^{-1} \left(1 + \frac{\tau}{S^2 \tau_D} \right)^{-2}$$
 (2.15)

where S is the structure factor of the focal volume and τ_D is the diffusion time of the molecule. From the fit functions, the diffusion time, number of molecules, and the diffusion coefficient are extracted. [63, 64]. Other fitting models are shown in table 2-1. Cross-Correlation

Fluorescence cross-correlation spectroscopy (FCCS) is an extension of FCS and is used to determine the degree of binding using equation 2.16. It was first established in 1989 by J. Ricka and Th Kinkert using scattered light from non-fluorescent scattered particles.

[65] The technique gained popularity in 1997 when Schwille applied it to study DNA-DNA renaturation. [66, 67] FCCS curves are calculated using:

$$G_{rg}(\tau) = \frac{\langle \delta F_r(t) \delta F_g(t+\tau) \rangle}{\langle F_r(t) \rangle \langle F_g(t) \rangle}$$
(2.16)

where F_r and F_g , represent the different wavelengths of lasers. Unlike FCS, FCCS is not dependent on the diffusion of the particle. FCCS can monitor the co-localization of two different molecules. [64, 68]

Diffusion type	Fitting Function
3D diffusion	$G(\tau) = \frac{1}{N} \left(1 + \frac{\tau}{\tau_D} \right)^{-1} \frac{1}{\sqrt{1 + \omega_0^2 \frac{\tau}{\tau_D}}}$
2D diffusion	$G(\tau) = \frac{1}{N} \left(1 + \frac{\tau}{\tau_D} \right)^{-1}$
2D diffusion for elliptical Gaussian profile	$G(\tau) = \frac{1}{N} \left(1 + \frac{\tau}{\tau_D} \right)^{-1/2} \frac{1}{\sqrt{1 + \frac{\tau}{S^2 \tau_D}}}$
2D diffusion with triplet	$G(\tau) = G(\tau) \left[1 + T (1 - T)^{-1} exp \left(\frac{-\tau}{\tau_{Tr}} \right) \right]$
2D diffusion with blinking	$G_B(\tau) = G(\tau) \left[1 + \frac{c_{dark}}{c_{bright}} e^{-k_{bl}\tau} \right]$
2D diffusion with two-component	$G_{2C}(\tau) = \frac{1}{N_{tot}} \frac{q_1^2 Y_1 G_1(\tau) + q_2^2 Y_2 G_2(\tau)}{q_1 Y_1 + q_2 Y_2}$
ble 2-1 Fitting models [69]	

21

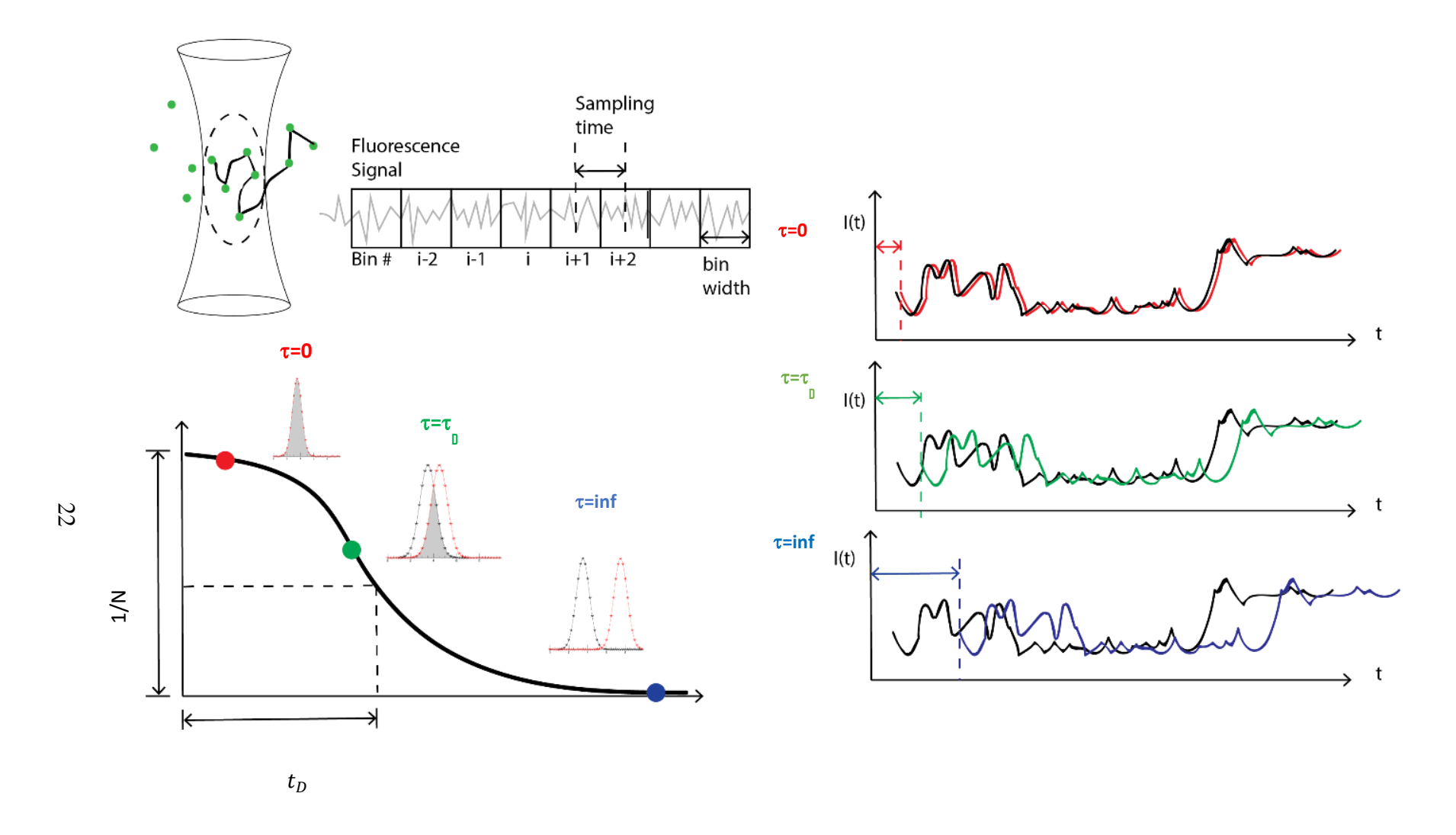


Figure 2-3 Development of an autocorrelation curve.

2.3 Introduction to Fluorescence

Provided that the FCS set-up is not time-dependent, the FCS measurements are sensitive to the fluctuations of the concentration and the photophysical properties of the fluorophores in the sample. [70] The Jablonski diagram shown in figure 2-4 describes the process of how absorption, fluorescence, and phosphorescence work. Fluorophores are excited by external radiation, which causes the molecules to transition from a ground state to an excited state. Singlet electronic states are identified in the graph as S_0 , S_1 , S_2 , and the triplet states are T_1 , T_2 (the names refer to the number of electronic spins). Each electronic state is associated with a vibrational level.

Once the molecule is excited by a wavelength, the photon goes into a vibrational relaxation, S_1 , or internal conversion before it enters a ground state. As this process occurs, energy is released in the form of emission- this phenomenon is called fluorescence. The energy released from the fluorophore is less than the energy of the wavelength absorbed. Excitation into a higher vibrational state is known as the Stokesshift. Some photons can go from the S_1 into the T_1 before relaxing into the ground state — this process is known as phosphorescence.

Phosphorescence occurs on the order of 10^{-4} up to seconds and is described as a delayed process. It is important to know that transitions of the electron states occur only for specific molecules and only if excited by a specific wavelength. Hence, proper dye and wavelength selection are key to perform fluorescence experiments. [71, 72, 73, 74]

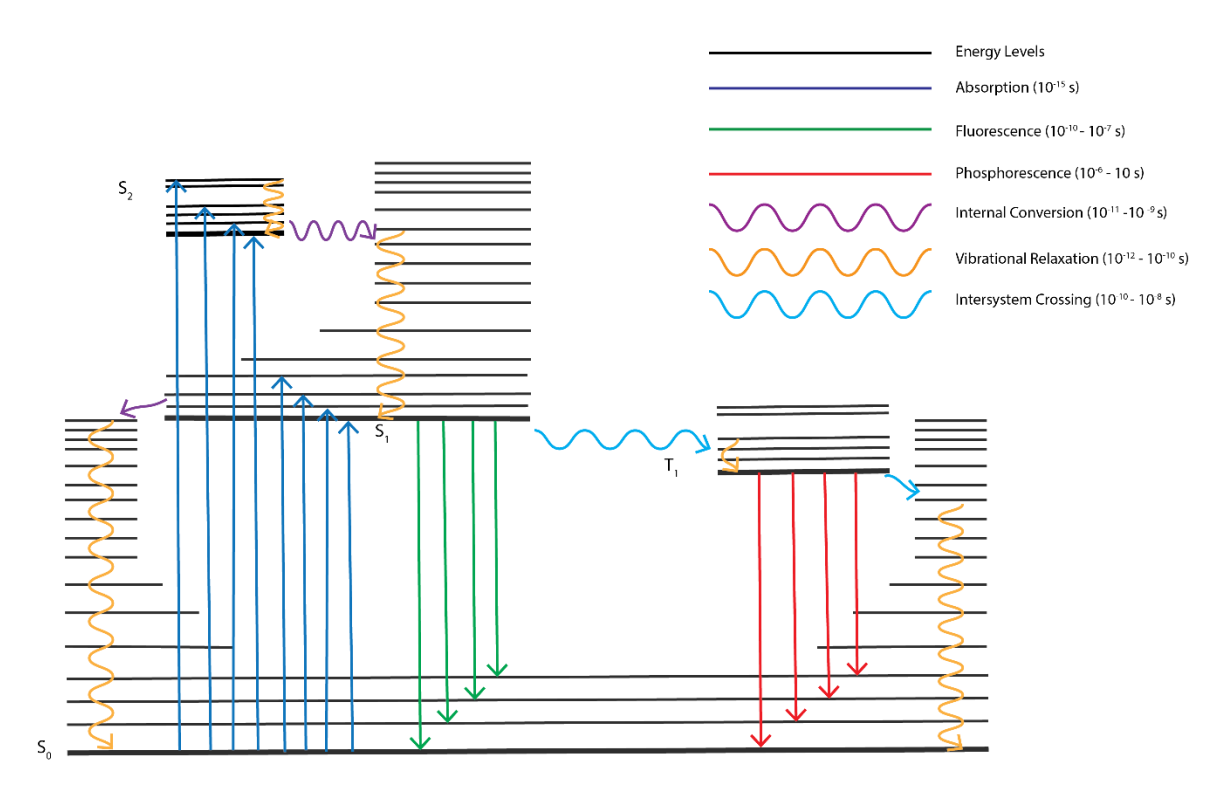


Figure 2-4 The Jablonski diagram gives a visual description of the different energy levels that occur during the excitation of a fluorophore.

2.4 Considerations in Performing FCS Experiments

2.4.1 Dye Selection/Fluorophores

The quality of FCS measurements depends on the signal to noise ratio (SNR); therefore, proper dye selection is important. The choice of dye is limited by the setup, i.e., the laser wavelength and filter sets that are available in your system. Each fluorophore has different spectrums of light that can be absorbed- this is called the absorption or excitation spectrum. For good signal to noise, it is crucial to select a photostable dye that is 1) bright, 2) has a high quantum yield, and 3) high extinction coefficient. While the correlation function is independent of the brightness, the SNR relies on the ability to see over the background. Ideally, a good dye survives 10^6 excitation cycles before it is

subjected to the process of photobleaching. Photobleaching is the process of the dye permanently losing the ability to fluoresce over time due to chemical damage. The quantum yield is related to the number of photons emitted divided by the number of photons absorbed.

$$Q = \frac{number\ of\ photons\ emitted}{number\ of\ photons\ absorbed}$$
(2.17)

Though photobleaching is a concern frequently in immobile molecules, bleaching can still affect slower diffusing molecules and can impact FCS curves – usually in the millisecond range. Photobleaching can limit the statistical accuracy of the detection; therefore, it is important to choose a dye with a high quantum yield or decrease the exposure of light over time. Longer exposure to light can induce photobleaching over time. [75]

Photobleaching can affect the curve by decreasing the diffusion time, therefore, increasing the diffusion coefficient. Moreover, the high intensity of the laser can cause the emission to go into the triplet state. During this process, the dye goes into a dark state and cannot emit any fluorescence. Like photobleaching, the triplet state can limit emission, therefore, affecting processes that occur in the microsecond range. [76, 77, 78, 79, 80]

2.4.2 Sample Concentration

Concentration is important in maintaining good SNR. Highly dilute concentrations for experiments range from $\sim 10^{-10}$ M to $\sim 10^{-6}$ M for a diffraction-limited volume. As the concentration increases, fluctuations become smaller in the observation volume,

decreasing the amplitude of the correlation function (figure 2-2). Because the amplitude of the correlation is inversely proportional to the number of molecules, it is important to maintain a small number of molecules in the confocal volume to observe a correlation with a significant amplitude. [48, 75, 81] However, successful attempts to monitor higher concentrations have been made at concentrations up to $38 \mu M$ [82, 83]. Increasing the concentration by a factor of *R* will increase the intensity by a factor of *R*. Also, it is important to note that high concentrations can cause saturation or damage to the detector.

2.5 Signal to Noise by Time Scale

It is essential to understand the contributions of errors in FCS measurements from systemic and random noise in order to understand the significance of the results. [58] Factors that can affect the signal to noise are detector afterpulsing, Poisson noise, and correlated fluctuation noise (figure 2-5). In order to capture the fluctuations, the correlator must run at a minimal sample time, i.e., small bin sizes. Understanding the origin of SNR will allow for optimizations in the FCS set up.

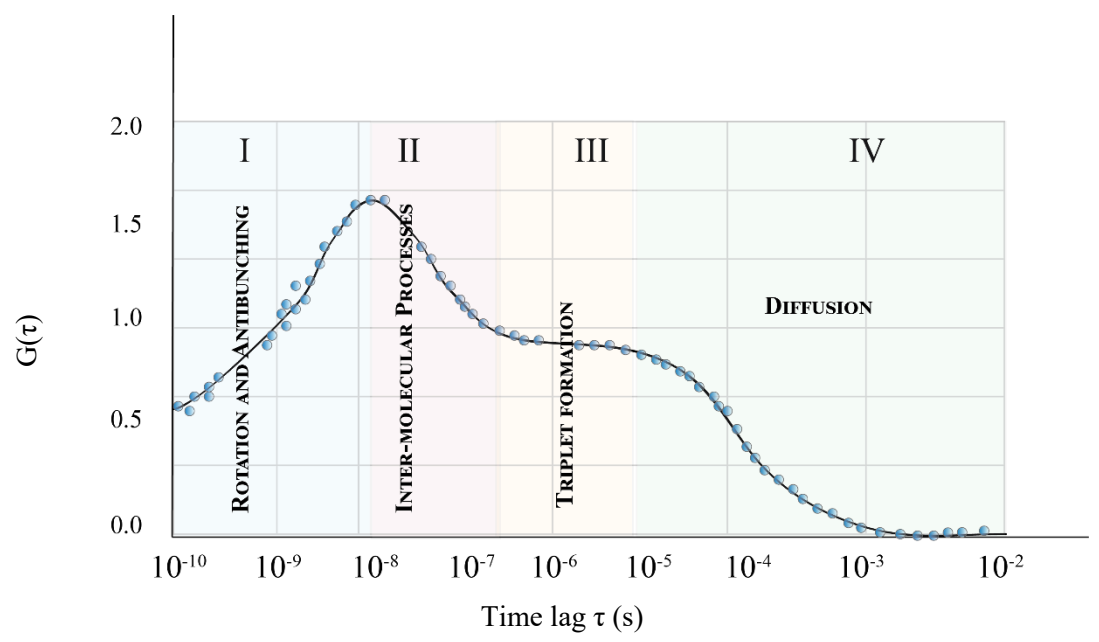


Figure 2-5 The areas at which noise can affect the curve overtime. Region I – rotation and antibunching, Region II – inter-molecular processes, Region III-triplet formation, Region IV- diffusion

2.5.1 Nanosecond time scale (Region I)

2.5.1.1 Photon antibunching

Antibunching results from the dye lack of ability to emit photons. Therefore, it will take time to emit a second photon – leaving long gaps between photons. Antibunching is often observed as a dip in the amplitude of the correlation curve. However, relevant FCS time scales are in the microsecond timescale. Therefore, antibunching is often not observed in most FCS measurements. [84, 85]

2.5.2 Microsecond time scale (Region II- III)

2.5.2.1 Detector Afterpulsing

Afterpulsing is a characteristic of the design of the photon detector and can affect the sensitivity and output of the detector. It arises from the feedback of events that occur due

to the nonlinearities of the detector. This feedback leads to an increase in the number of photons detected, thus, affecting the amplitude of the correlation curve. Therefore, it can be challenging to determine the average number of molecules in the volume.

Afterpulsing can be limited by using special circuits that reduce the bias voltage or by using cross-correlation of detectors. [86] Cross-correlation can lead to longer measurement time and alterations of the setup because two detectors will need to be aligned. Other groups have investigated eliminating afterpulsing using one detector using autocorrelation [87] Afterpulsing can also be corrected using a correction factor (equation 2.18) and calibration method. [84, 88, 89]

$$correction factor = \frac{1}{1 - (t_d \times C_R)}$$
 (2.18)

where t_d = module dead time and C_R is the output count rate.

2.5.2.2 Poisson Noise or shot noise

Random errors can result from Poisson noise or shot noise, which can dominate the microsecond region. The SNR is dependent on the particle brightness and the size of the correlator binning, i.e., time resolution or sampling time. Curves dominated by Poisson noise can often be hard to fit. Shorter sampling times can introduce more Poisson noise; therefore, to decrease the amount of noise, it is suggested to use larger bin sizes.

Although larger bin sizes will cause a loss in data, it allows the correlator to present smoother curves as Poisson noise is decreased with increasing τ . Correlators are often fixed to nanosecond bin sizes enabling the likelihood of Poisson noise; however, many FCS experiments are interested in the microsecond region because of the sample diffusion time. The SNR in this region is calculated by:

$$\left(\frac{S}{N}\right) = \frac{1/m}{\sqrt{var(g(v))}} = \sigma\sqrt{T\Delta t}$$
 (2.19)

where m is the number of fluorophores, σ is the mean fluctuation, g(v) is the correlation, T is the measurement time, and Δt is the minimum sampling time. Therefore, the signal is dependent on the measurement time T and the sampling time Δt . At low concentrations, the signal to noise is equal to \sqrt{N} .

2.5.3 Millisecond time scale (Region IV)

2.5.3.1 Correlated fluctuation noise

On the millisecond to second scale, the correlation function decays due to lateral diffusion of the molecules. As the fluorophore brightness increases, the SNR will increase, which will allow for a high-count rate. Signal to noise depends quadratically on the dye brightness. To maintain the same SNR, as the excitation power is increased by a factor of R, the measurement time must increase by a factor of R^2 . [83] One can increase the laser power at the expense of possibly photobleaching the sample or saturating the detector.

In keeping, decreasing the number of fluorophores will increase the amplitude of the correlation curve. Koppel presented an approximation of the standard deviation by assuming an ideal signal to noise situation, i.e., high particle count, negligible background count. Koppel concluded that particles emitted in consecutive dwell times would become correlated over time. [90] The signal to noise in this region is calculated by:

$$\frac{S}{N} \approx \frac{q\sqrt{N}}{\sqrt{1+q^2}} \tag{2.20}$$

where N is the number of time bins collected, q is the average number of photons collected from a single fluorophore, and N is the number of bins. Substituting $N \approx \sqrt{T}/\Delta t$ and $q = \sigma \Delta t$, the signal to noise is:

$$\frac{S}{N} \approx \frac{\sigma\sqrt{T\Delta t}}{\sqrt{1 + \sigma^2 \Delta t^2}}$$
 (2.21)

In conclusion, particle brightness, sampling time, and the total measurement time are important in maintaining a suitable signal to noise. Proper assembly of the confocal system and correlator design are essential in producing quality FCS curves. [89, 91, 92]

3 Software Design and Confocal

Microscope Assembly

3.1 Introduction

As stated in chapter 2, the signal to noise is vital in obtaining FCS curves. This chapter describes the methods that were used to optimize our setup by developing an FPGA correlator that can run a multi tau correlator and dual correlator, simultaneously.

Assembly of the confocal system is discussed, as well.

Calculations of the correlation curves are obtained either using a hardware or software correlator. Hardware correlators provide speed with the combined ability of real-time calculations. Software correlators are a more cost-effective option and offer the

flexibility of user design. There are several software correlators that are established with various algorithms. A simplified algorithm that is utilized by both hardware and software correlator is the multi tau technique, which was invented by Schtazel [93, 94, 95, 96].

Multi tau correlators can calculate a full FCS curve by using a binning technique, which cuts down on the number of data points to calculate (roughly 178 data points). The correlator is based on multiple linear correlator blocks. Each block doubles in time resolution from the latter block. Other algorithms use various methods of binning techniques, such as exponential binning [97]. The multi tau technique has some disadvantages, such as a triangular averaging effect, and aliasing can occur. Because of aliasing, the multi tau correlator has difficulty acquiring data with single molecule techniques due to low concentrations that are used in experiments. Signal to noise varies based on the brightness and binning resolutions of the multi tau correlator. One solution to overcome these disadvantages is to use a linear correlator.

Linear correlators maintain the same time resolution throughout the calculations of autocorrelation. The simple correlation histogram (SCH) created by Yang is a less complicated algorithm compared to the multi tau software. It calculates the correlation function on a linear scale. However, the disadvantage of this software is the number of resources it takes to calculate a full correlation curve. A correlator requires 10⁷ points and bin spaces to calculate an FCS curve. In continuing, SCH is often prone to overflows from high count rates of photons. Several dual correlator designs exist that provide both linear and multi tau techniques to overcome this disadvantage [2, 3].

We present a Field Programmable Gate Array (FPGA) dual linear and multi tau software, which allows the user to select between bulk and single molecule experiments.

We use LabVIEW FPGA software, which allows pipelining and parallelism of our algorithm, to calculate correlation functions in real-time.

3.2 Types of Correlators and Background of the Designs

3.2.1 Multi Tau correlator

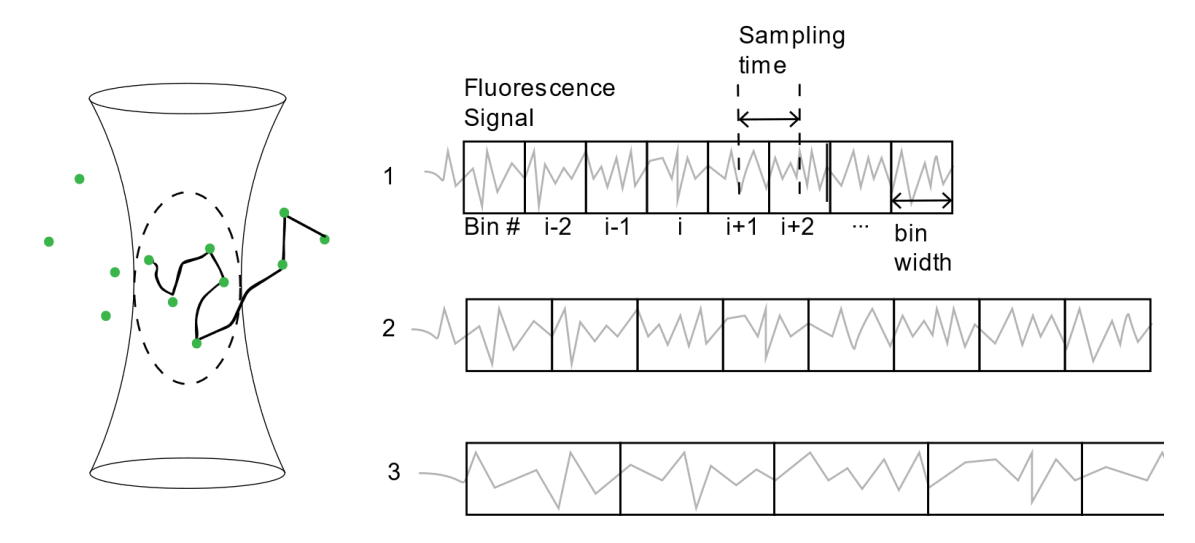


Figure 3-1 The sampling time doubles for each linear correlator 1, 2, and 3. In short, the multi tau correlator is a series of linear correlators at different sampling times. Linear correlator 1 is sampled at 1μ s, linear correlator 2 is sampled at 2μ s, and the correlator 3 is sampled at 4μ s, etc.

The multi tau correlator is a fast yet complex design that can calculate the autocorrelation over decades in just a few data points (figure 3-3). [98] The correlator can be divided into two parts: the scheduler and the correlation. The correlator is broken down into several blocks (k). Each of the blocks represents a linear correlator and are arranged in an assembly line fashion. The scheduler tells the correlator which linear block to execute. In short, each correlator block must operate twice before the latter block is executed. Therefore, the time resolution for each linear block is doubled, i.e. block 1 = 25

ns, block 2 = 50 ns, block 3 = 100 ns etc. Each linear block consists of 8 linear correlator channels, except the first block, which consists of 16 channels. The intensity is received at the first block, and the data is shifted in the linear bin channels to the right. The last two bins of the block are summed together and added to the first channel, l, of the next block (k+1).

The data received at the first channel of each block is known as the zero-delay data. The zero-delay data is added to a direct monitor or the undelayed monitor, $M_{dir,k}$. Data that is shifted to the right of each channel is also added to what is called the delay monitor, $M_{del,k,l}$. The direct monitor and the delayed monitor are used for normalization. The autocorrelation function is calculated by multiplying the delay signal with the zero delay and accumulating the values. Once each block completes the set number of executions, the data is then sent to the computer. In short, the main steps of the multi tau algorithm are:

$$1 \times \Delta t_k + \frac{1}{2} \Delta t_{(k+1)} + \frac{1}{4} \Delta t_{(k+2)} + \cdots$$
 (3.1)

- Input the value at zero delay into the first channel of the block 1 and into the direct monitor channel
- 2. Add the zero delay value to the block preceding it
- 3. Shift channel values to the right
- 4. Sum the last two bins of each block and input it into the first channel of the block k+1
- 5. Multiply the value at zero delay, by the delayed value and sum the value into an accumulator. This will be your G_x .

3.2.2 Linear correlator

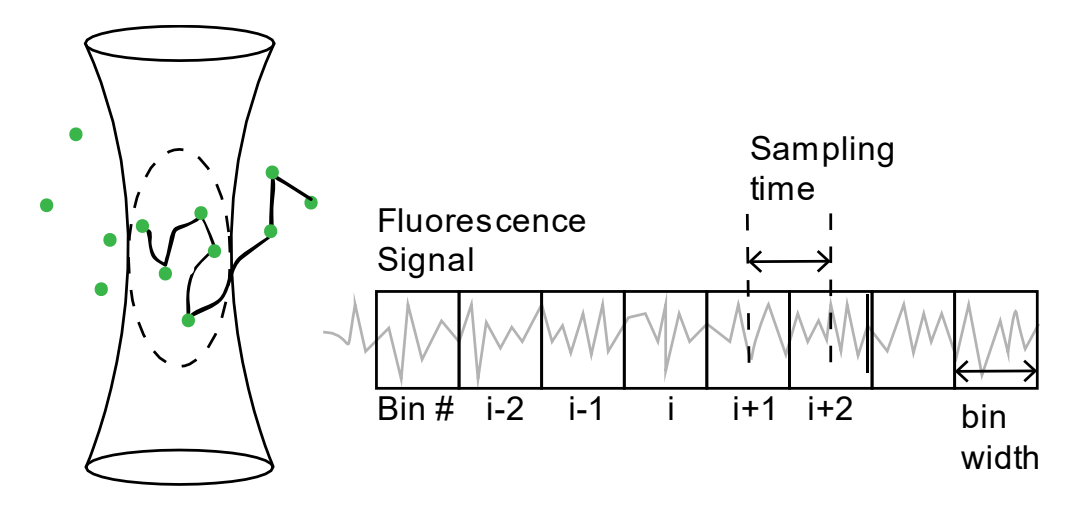


Figure 3-2 In the linear correlator, the sampling time remains constant. Therefore, if a correlator has a sampling time of 1μ s and the user would like to calculate up to 1 second. It would take 10^6 data points to calculate the correlation curve.

Unlike the multi tau correlator, a linear correlator maintains the same time resolution throughout the calculation. We decided to use the Simple Correlation Histogram (SCH), a technique developed by Yang [99]. The SCH algorithm offers a more straightforward design. Instead of taking the intensity, the inter photon or delay times are used. The delay time is the time that it takes for a photon to arrive. Yang uses a lookup table to update the autocorrelation function.

As the delay time enters the correlator, the autocorrelation is updated with a 1. Once the next delay time enters the correlator, that time is then added to the previous time, and that arrival time and correlation value are updated with a 1. This design will allow for the calculation of the full correlation curve. However, it is not necessary to calculate the full curve, and due to the number of data points, Yang eventually had to use a binning technique.

3.2.3 Dual Correlator

Dual correlators combine linear and multi tau correlators together into one. The advantage of this design is that the linear correlator can calculate larger bin sizes and decrease the Poisson noise from the signal. Table 3-1 is a list of a few software and hardware correlators that are available.

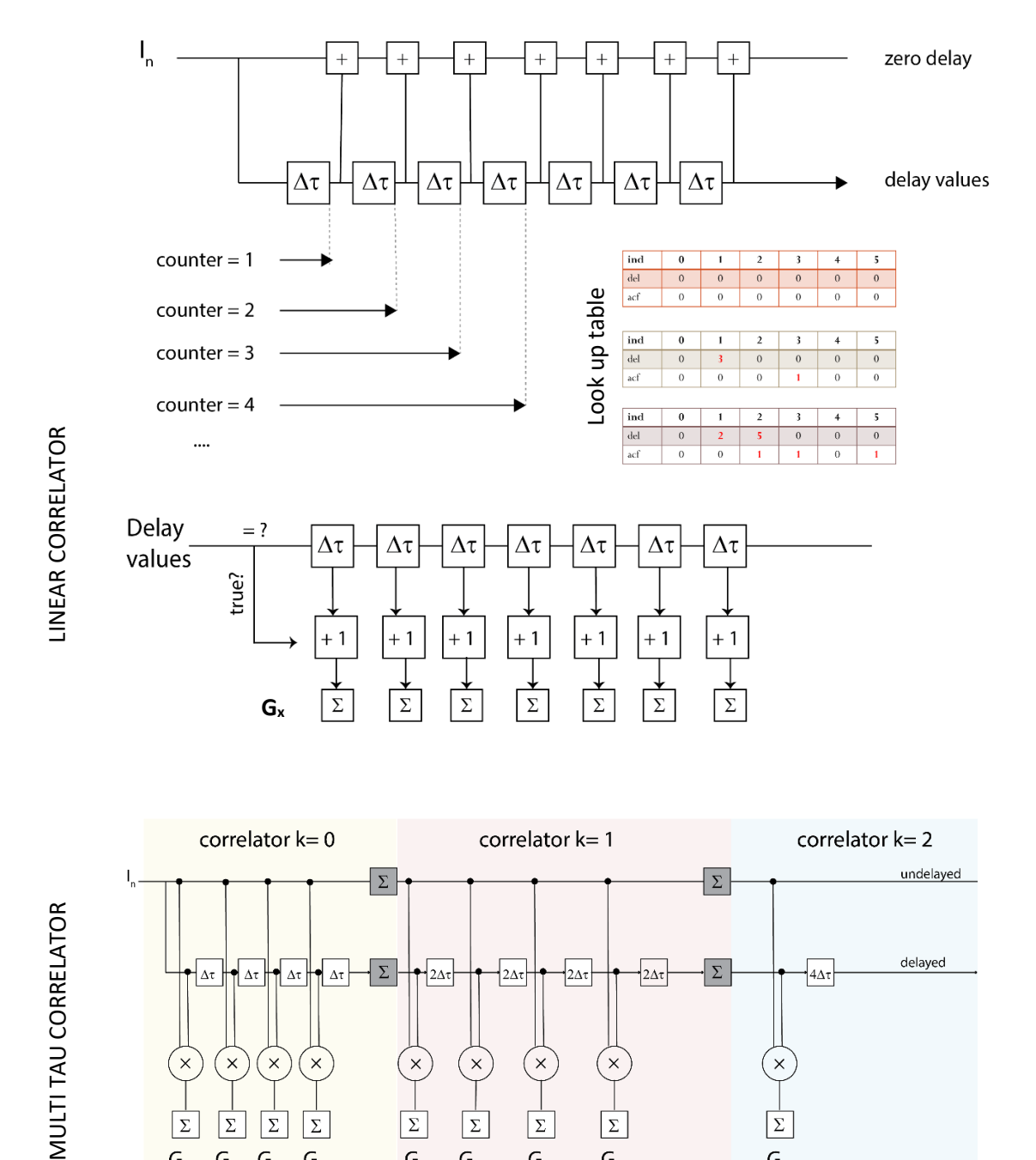


Figure 3-3 Top: the design of the linear correlator. Bottom: The design of the multi tau correlator. The design of the dual correlator is the linear correlator combined with the multi tau correlator. The two correlators are run simultaneously.

Σ

 $G_{k,3}$

Σ

 $G_{k,4}$

Σ

 $G_{k,1}$

Σ

 $G_{k,1}$

Σ

 $G_{k,2}$

Σ Σ Σ

 $G_{k,2}$ $G_{k,3}$ $G_{k,4}$

	,
ζ	ĸ,
-	,

Paper	Software	Time Resolution	Sample
Multiplexed multi-tau auto and cross correlators on FPGA [100]	Multi Tau	100 ns	W6/32 antibodies double-labeled with Alexa Fluor 488 and cy5
10 ns software correlator for photon and FCS [101]	Dual	10 ns	40 nm polystyrene spheres
Vectorized triple correlation [102]	Multi tau	1μs	Proteins
A 4 ns hardware photon correlator [103]	Multi tau	4ns	Rhodamine 110
FPGA implementation of a 32x32 autocorrelator array [104]	Multi tau	10 μs	Simulation/beads (100 nm, 40 nm)
A fast, flexible algorithm for calculating correlations in FCS [105]	Linear	12.5 ns	DNA oligomers
25 ns software correlator for photon and FCS [106]	Dual	25 ns	73 nm polystyrene spheres
High-throughput FCS using an LCOS spatial light modulator and an 8 × 1 SPAD array [107]	Multi tau	50 ns	Rhodamine 6g (Water/Sucrose)
Fast calculation of fluorescence correlation data with asynchronous time-correlated single-photon counting [108]	Linear	100 ns	Bead solution
F2Cor: fast 2-stage correlation algorithm for FCS and DLS [109]	Dual	1μs	TMR
High countrate real-time FCS using F2Cor [110]	Dual	1μs	TMR
Real-time data acquisition incorporation high-speed software correlator [99]	Linear	25 ns	RG6 in water

Table 3-1 A list of available software correlators and the samples that were used to verify the systems.

3.3 Dual FPGA Correlator Design

3.3.1 FPGA

A field-programmable gate array (FPGA) – known as the target- is used to acquire our data and calculate the correlation functions in real-time. The FPGA was selected for speed and parallelism- which allows the software to multitask. The FPGA hardware consists of a 40 MHz base clock which controls the time resolution of our software. The FPGA is also reconfigurable- allowing for the addition of other software applications. Programming on the FPGA helps decrease the processing load for the computer- known as the host. Our host side is used to display the correlation curves and handle other calculations that are not available on the FPGA.

FPGA Terminology		
FIFO	a buffer that is used to transfer data throughout the software	
Memory	where the FPGA stores data	
Target	for this application is the FPGA card	
Host	for this application is the computer	
C module	a digital input/output module which interacts with the detector to send or receive a signal	

Table 3-2 FPGA terms

3.3.2 Dual Correlator FPGA design

Like Magatti and Schuab software, our design will allow for a linear correlator for the beginning of the curve, and a multi tau correlator for the latter part of the curve. [106, 110] We use a NI 9155 Compact RIO Chassis, which features a Virtex-5 LX85 FPGA card [111]. The chassis offers flexibility to add up to eight C-modules for digital and

analog signals. We use the NI 9402 C module (figure 3-4) to receive the digital TTL (transistor-transistor logic) signal from the detector at the speed of 55 ns.



Figure 3-4 NI 9402 C module receives the signal from the detector.

In our design, we reserved a fixed 1024 bins and calculated the correlation function on the FPGA. Creating an array larger than 1024 elements required a lot of memory resources, however, from Schuab, Yang, and Magatti's design, it appears that 1024 bins will be substantial in calculating the correlation. The focus of our SCH FPGA design is to overcome the buffer overflows that occur due to the massive surge of photon counts. Therefore, instead of calculating the correlation on our host computer, we choose to calculate the correlation mainly on the target FPGA. This technique reduces the

amount of computer processing that would slow the display of the correlation, and therefore cause overflows. The delay times are transferred to another loop where the software calculates the correlation.

3.4 FPGA Linear Design

3.4.1 Target

- 1. In the first loop, the Input module, NI 9402, receives the signal from the APD and calculates the delay times received.
- 2. A FIFO reads the input delay times and sends it over to the second loop.
- 3. The second loop is used to calculate the delay times. The delay times are read from the FIFO and are 1) checked to ensure that the value is not higher than the max time and 2) checked to ensure that the delay time is not 0.
- 4. The first delay time is stored in the memory block as the first value 0 on channel 0.
- 5. A counter is used to count the number of correct delay times. This counter allows the software to keep track of what values to calculate.
- 6. Other software checks include: 1) checking if the delay value is at maximum, 2) deleting that delay value that is over max value, i.e., setting that value to zero, and 3) resetting the delay values.
- 7. As the delay times are calculated, the values are delivered to a FIFO, where it is transferred to the third loop.
- 8. The third loop is used to calculate the correlation function. A memory block is used as a simple lookup table. The delay values select the memory spot or time value to increment by 1.

9. Once the calculation is completed, the software resets all the delay times, correlation values, and empties any remaining delay times from the FIFOs.

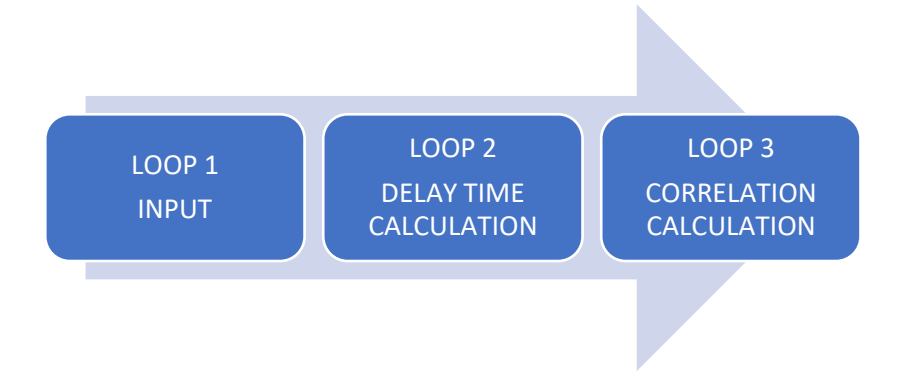


Figure 3-5 Flow of FPGA Linear Correlator

A critical factor in the linear design is eliminating buffer overflows. Buffers on the FPGA are limited to 1024 values – a small amount. This limitation can cause errors in the calculations and a loss of photon delay times. Buffer overflows are caused by large bursts of data that are received at high speeds. Although the software runs at 25 ns, the time to calculate the delay times can cause a "traffic jam" in the data, because the loop is reading slower than the data is writing. The software resolution can be adjusted to a slower time scale to allow a steady flow of data. Though the resolution becomes slow, most FCS curves sample at $1~\mu s$ resolution-eliminating higher resolution values. This is due to afterpulsing from the detector and the triplet state from the dye that contributes to the noise at the beginning of the FCS curves. Therefore, the values are read into the buffer slower, allowing for the calculations to occur at 25 ns speed.

Another factor that allows the linear software to eliminate buffer flow is calculating a short time range of the curve. The software can calculate 1024 correlation functions; however, the user can adjust the time range of values to calculate. For

example, a time resolution of 1 μ s, with a max value of 150 μ s, will allow only 150 correlation functions to be calculated. Nevertheless, the most crucial factor is the time it takes a molecule to diffuse through a solution. Considering that biological molecules travel in the microsecond range, the software can handle the data flow. A software counter totals the number of buffer overflows and sends a warning to the user if any overflow occurs.

In parallel, the multi tau algorithm receives the intensity or the number of photons counts over a given period. We patterned the design based on Moscar correlator, where we count the number of times the block has executed twice using a mod technique [100]. The software can detect whether an even number occurs, and the block counter is incremented. Data is received every other clock cycle, allowing the multi tau correlator to be calculated entirely on the FPGA.

3.4.2 Host side

Plotting and normalization of the correlation function occur on the host side. The data is normalized on the host side using equations 3.2-3.4 for the multi tau correlator:

$$G_{\tau_{k,l}} = \frac{T}{2^{k-1}} \frac{G_{k,l}}{M_{dir,k} M_{del,k,l}}$$
(3.2)

$$M_{dir,k} = \frac{1}{M} \sum_{j=1}^{M} n_j n_{j-k}$$
 (3.3)

$$M_{del,k,i} = \frac{1}{M} \sum_{j=1}^{M} n_j$$
 (3.4)

The linear correlator is normalized by dividing by the count rate. Weights are applied to the normalization function to merge the linear curve with the multi tau curve. Linear data points from 1 μ s to 150 μ s are used, while data points greater than 150 μ s are plotted by the multi tau correlator. This range has been successfully tested out by Magatti [106]. The linear correlator is normalized using equations 3.5-3.6:

$$G_{tau} = G_{\tau} + 1 \tag{3.5}$$

$$G_N = \frac{G_\tau}{countrate^2} + 1 \tag{3.6}$$

where G_{tau} is the correlation values at delay time τ .

The linear and multi tau correlators are merged into one dual correlator on the host side. In figure 3-5, the dual correlator shows smooth binning compared to the multi correlator. The dual correlator was able to handle count rates up to 100kHz. This outcome is explained in chapter 4.

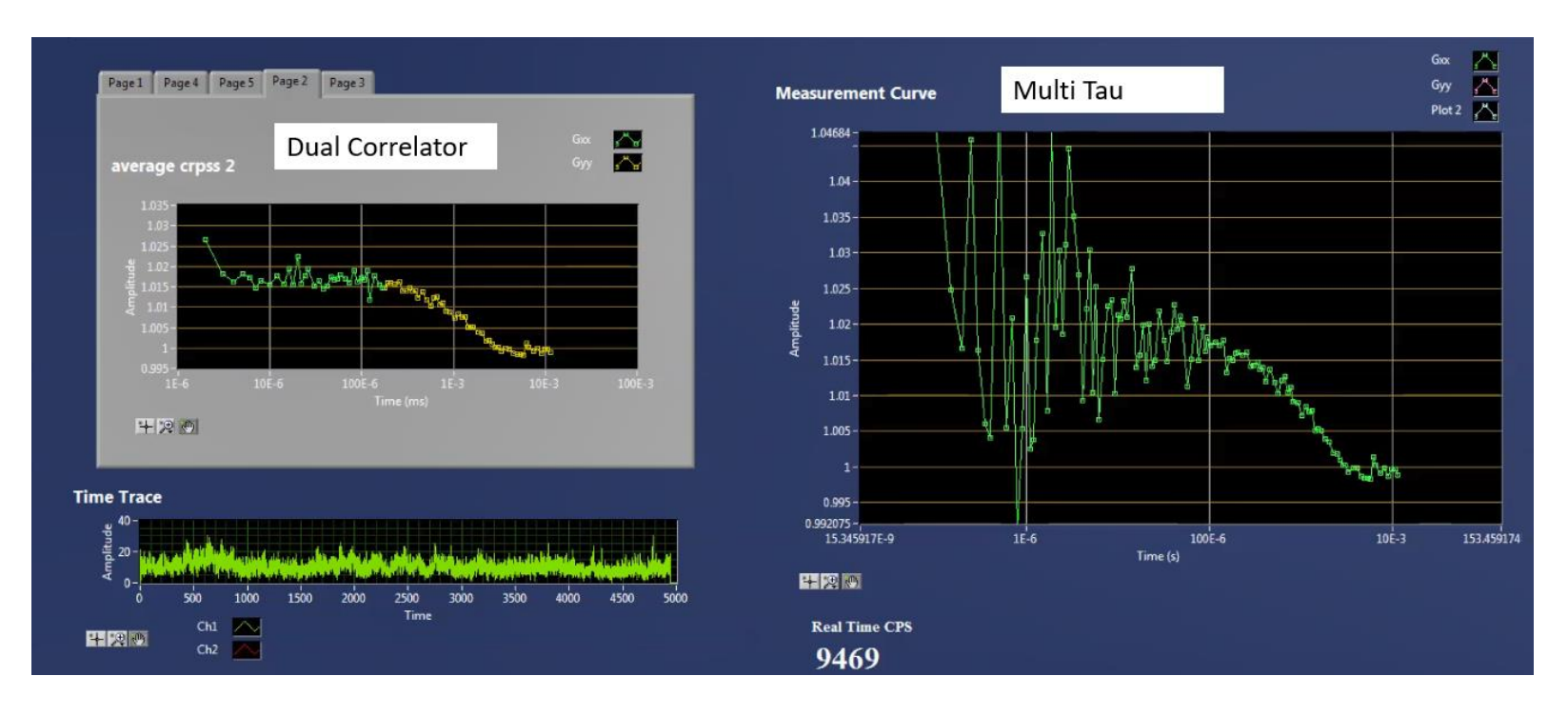


Figure 3-6 Screenshot of the Dual correlator and the multi tau correlator. The dual correlator gives a smoother look to the curve because of the larger bins set to microseconds, while the multi tau correlator is sampled at 50 ns and is noisier because of the smaller bins. The yellow data points on the dual correlator represent information from the linear correlator, while the green data points are from the multi tau correlator.

3.5 Hardware Set-Up of Confocal Microscopy

PARTS LIST

M1 – M4 M5- M6	1-inch mirrors 2-inch mirrors
Laser	Compass 215M-75 532 nm laser, 75 mW
Half Wave (HWP) Beam Splitter (BS)	Thorlabs Zero-Order Half-Wave Plate, 532 PBS12-532 - 1/2" Polarizing Beamsplitter Cube, 532 nm
L1	LA1560-A - N-BK7 Plano-Convex Lens $f = 25.0 \text{ mm}$
L2	Thorlabs, LA1509-A Plano-Convex f = 100.mm
L3	Newport KBX076 N-BK7 Bi-Convex Lens f = 200 mm
L4 and L5	Thorlabs ACL1815-A - Aspheric Condenser Lens, f=15 mm
Microscope	Olympus IX50
Objective lens (OBJ)	Olympus UPlanSApo 60 x/1.20 W
DM1 Filter Cube BP Filter Cube Raman Filter (RF)	532 nm RazorEdge Dichroic laser-flat beamsplitter 532 nm RazorEdge® ultrasteep short-pass edge filter Thorlabs
DM 2	Chroma Beam Splitter, 630 DCXR
Pinhole	Thorlabs P10D, P25D, P50D, P75D 6 mm Travel XY Translation Mounts
Fiber	P1-460A-FC-2 Single Mode Fiber Patch Cable, 2 m, 450-600 nm Thorlabs MBT613 - Single Mode Fiber Launch with FC- Connectorized Fiber Holder
Detector – APD 1 and 2	Perkin Elmer SPCM-AQRH-15
FPGA	NI 9155 Compact RIO Chassis Virtex-5 LX85 FPGA card NI 9402 Digital Input/Output
Relay (APD switch)	NI 9481 relay module and a 4-Slot, USB CompactDAQ Chassis

Table 3-3 List of Parts for the FCS Set-up

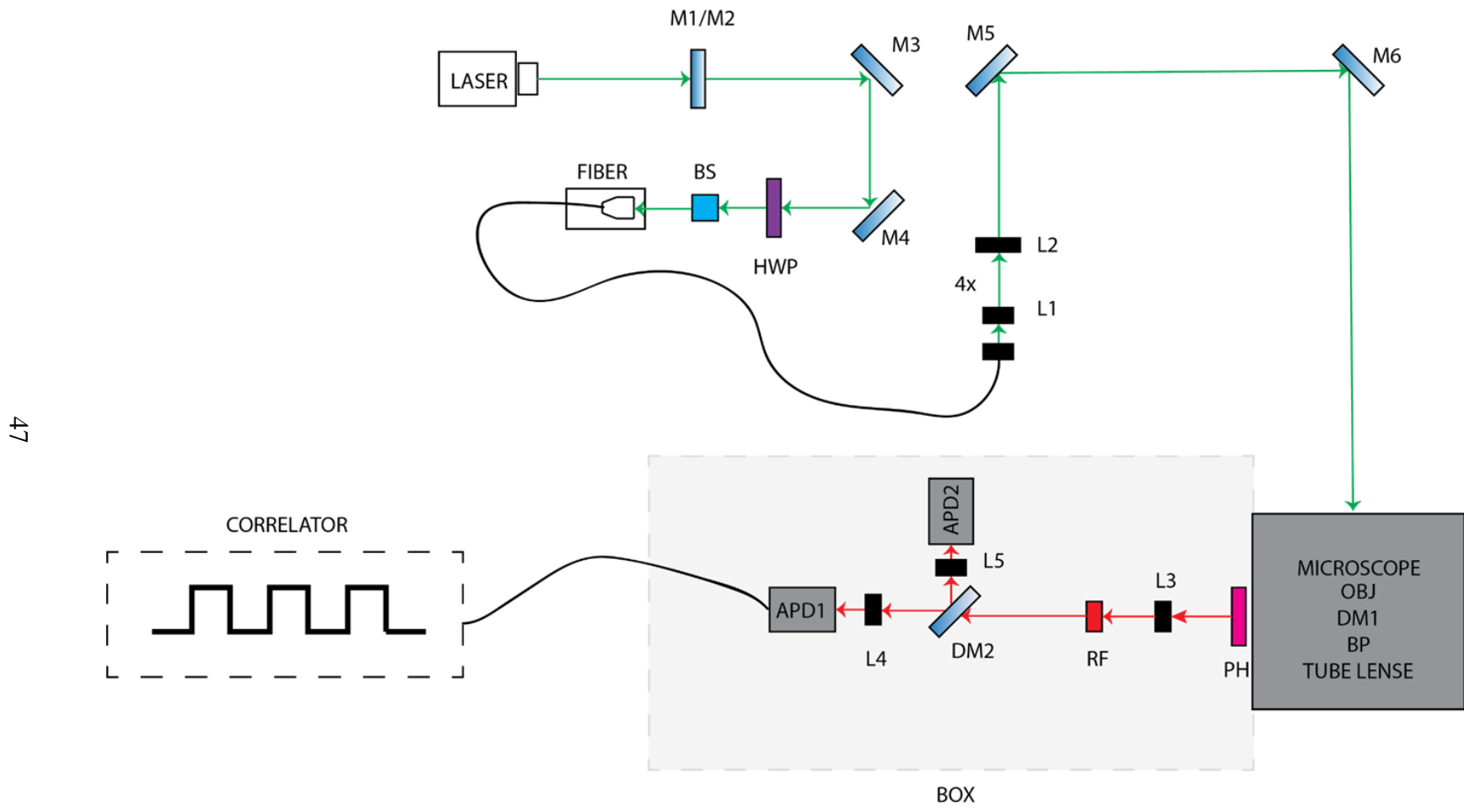


Figure 3-7 Layout of the FCS system.

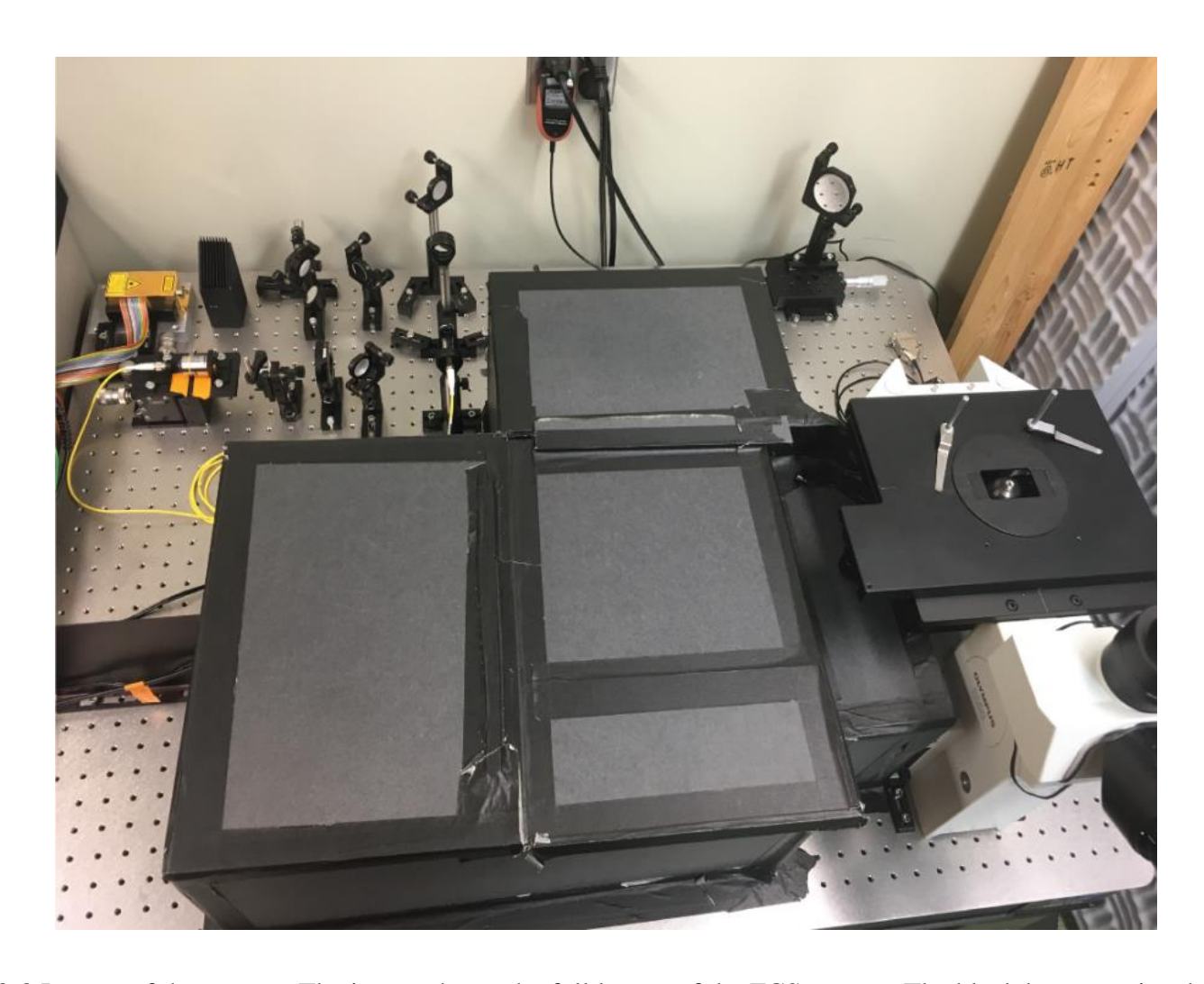


Figure 3-8 Layout of the system. The image shows the full layout of the FCS system. The black box contains the emission pathway. The box is used to eliminate light that could interfere with the emission pathway.

3.5.1 Excitation Pathway

A basic FCS setup is shown in figures 3-7 and 3-8. A one-photon excitation 75 mW 532 nm laser is used for excitation. The beam is reflected onto mirror M1, which is mounted on a 45° mount. The beam is reflected at a 90° on to M2, where it is reflected on to M3 and then M4. The beam is guided through a polarizing beam splitter which controls the laser power. An optical density filter can be used to vary the laser power. Next, the beam is guided into an objective and is coupled to a fiber optic. The fiber optic allows for the beam to be collimated. The objective lens of the fiber is mounted on a small stage, which is used to focus the beam into the fiber optic cable with the use of x-, y, and z screws. Fine adjustments are recommended as the alignment is sensitive to very slight changes in the x and y-direction.

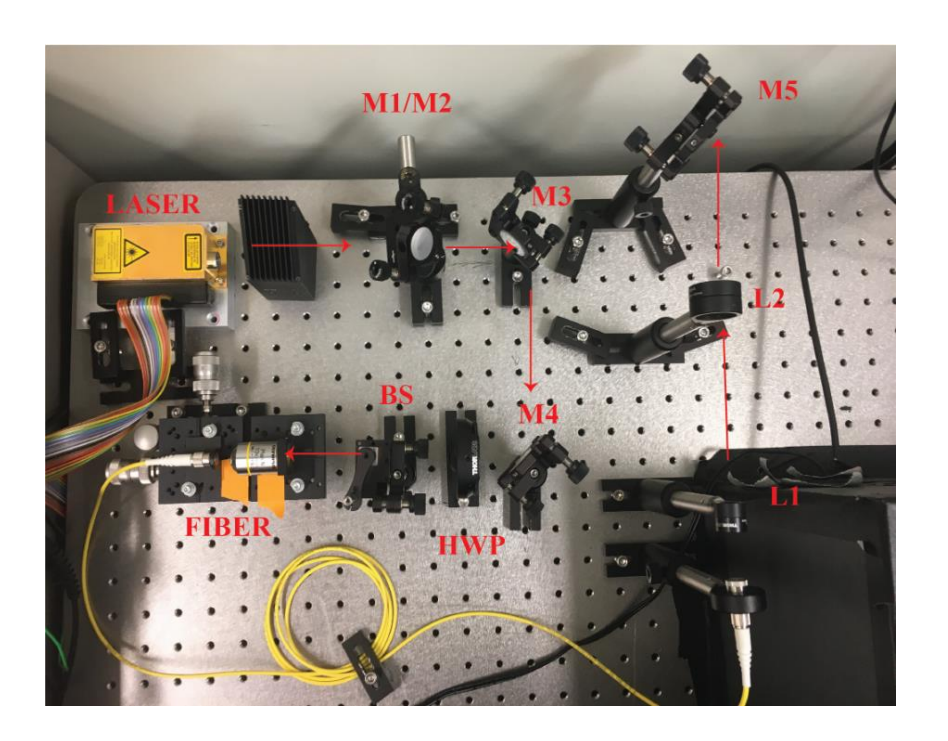


Figure 3-9 The image shows the alignment of the excitation pathway.

A telescope constructed from two lenses expands the beam. The focal lengths 25 mm (L1) and 100 mm (L2) of the lenses expand the beam 4 times, allowing to overfill the back of the objective lens. Overfilling the back of the objective lens decreases the artifacts in the data and helps maintain a gaussian shape. [112] The beam is reflected off M5 and is directed into the back of the microscope. The excitation beam is separated using a long pass dichroic mirror that reflects the beam into a 1.2 W 60x UPlanSApo objective lens and allows emission light to be reflected through the microscope. The dichroic mirror (DM1) reflects a laser light of <532 nm into the objective lenses while it passes longer wavelengths. Next, the emission light passes through another bandpass filter (BF), which blocks any excitation light that may pass through the dichroic mirror. The emission beam is directed into a telescope.

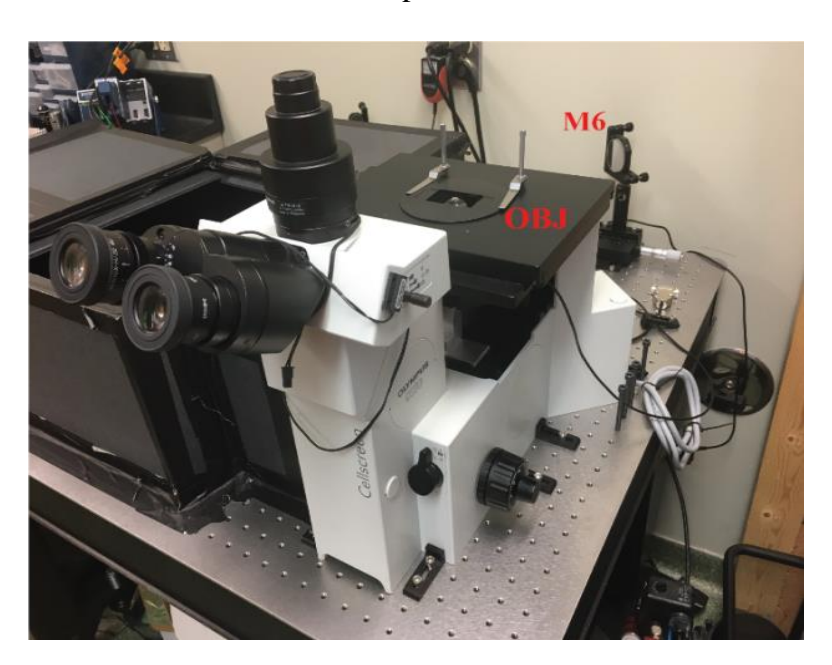


Figure 3-10 Image shows the placement of the objective lens, which is crucial for creating the confocal spot.

3.5.2 Emission Pathway

To begin the alignment of the emission pathway, a filter is used to back reflect the laser light into the emission pathway. The emission pathway is aligned with the back reflection first and then aligned with a highly concentrated Rhodamine 6G dye sample.

3.5.3 Alignment of the Pinhole

The pinhole size is dependent on the size of the numerical aperture of the objective lens, the wavelength of the excitation laser, and the focusing tube lens. The pinhole is often set to the size of 1 Airy disk:

$$Airy \, Disk = \frac{1.22 \cdot \lambda}{NA} \tag{3.7}$$

In our set up, we are using a 532 nm (λ) laser, with a 1.2 NA objective lens. Therefore, the focal diameter of the objective lens is 0.541 μ m. An "open" pinhole will allow more light to enter the emission pathway- helping to increase the signal. However, more out-of-focus light will enter the system.

In accordance, closing the pinhole will increase sensitivity in the x-, y-, and z-direction. The pinhole is roughly matched to the focal spot or the size of an airy disk (equation 3.7). [94] The microscope system is equipped with a 100 mm tube lens inside. The light is focused, and then the pinhole is positioned precisely in front of the collimated beam. The 100 μm pinhole is settled in a mount with an x,y,z micrometer. Slight adjustments can be made until the focused light is guided through the pinhole at optimal intensity. The procedure is repeated for pinhole sizes of 75 μm, 50 μm, and 25 μm until each pinhole position is centered at the focal spot.

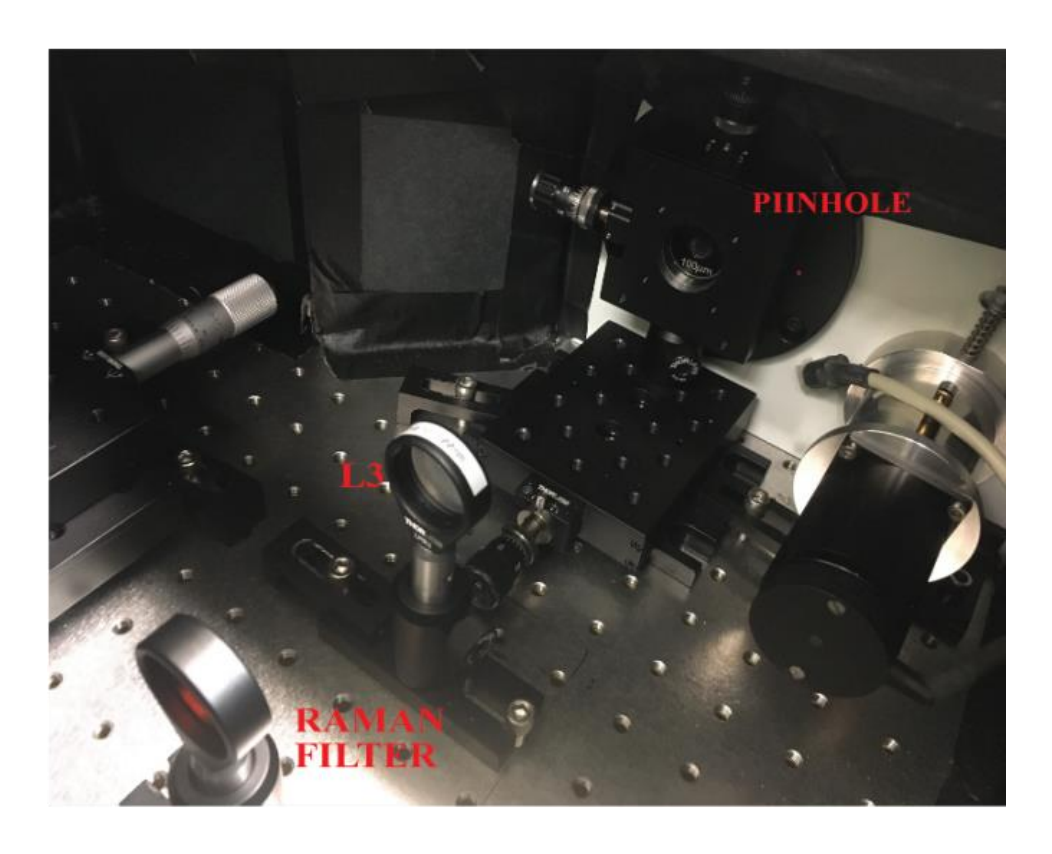


Figure 3-11 The pinhole helps create the confocal volume by eliminating out of focus light from the focal point. The emission light passes through the pinhole and is then collimated with the 200 mm lens (L3). Collimation of the light helps keep the beam from diverging. The Raman filter eliminates the Raman signal from the signal. The filter can have some effect in eliminating the necessary signal since the emission light and the Raman light overlaps.

The emission light is collimated with a 200 mm focal length lens and then guided through a Raman filter. A dichroic mirror (DM 2) is used to divide the signal if FCCS is needed. The light is collimated through a 15 mm focal length lens, where it is focused on the APD detector. Slight adjustments of the APD can be made using the micrometer to align the emission light onto the sensor (figure 3-11 and 3-12).

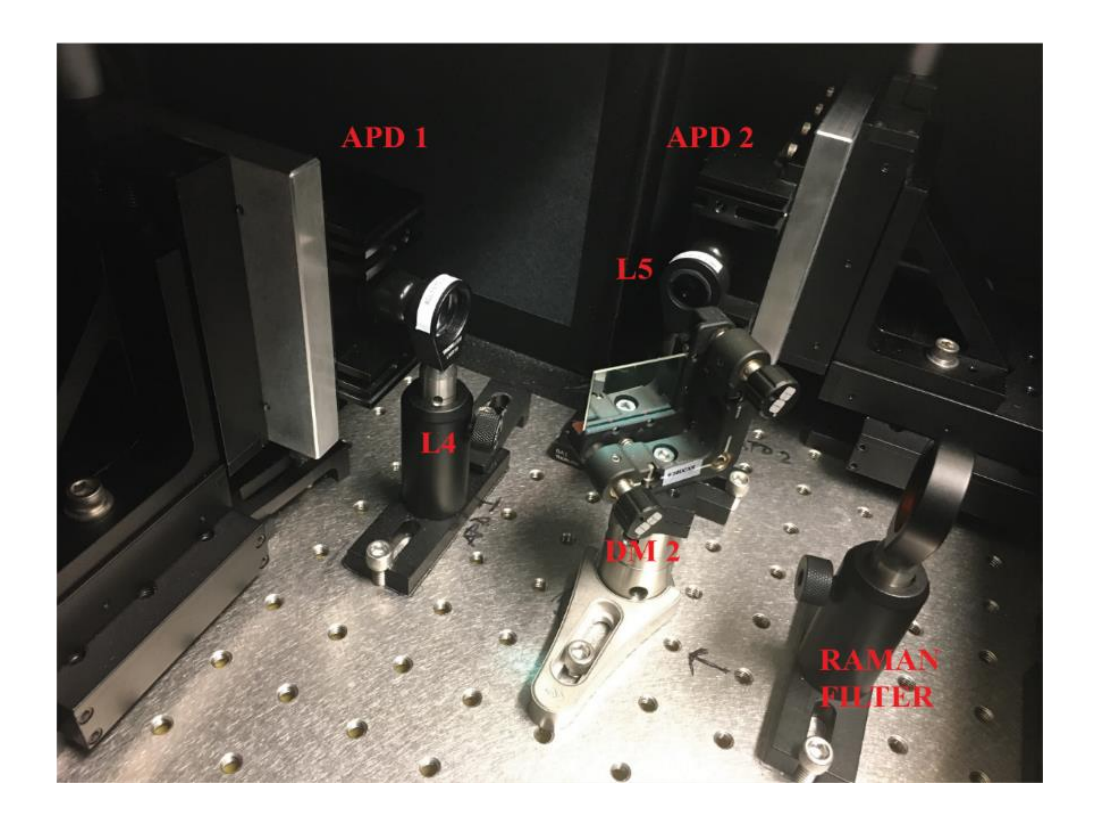


Figure 3-12 Emission pathway of the setup. The light is directed onto APD 1 and APD 2 using a dichroic mirror. In the FCCS setup, the dichroic mirror will separate the two signals.

The APD is connected to NI 9481 relay module and a 4-Slot, USB CompactDAQ Chassis, which is control by the LabVIEW software (figure 3-13). The software uses the relays to switch the APDs on and off (figure 3-14). Also, the software contains a safety switch, which triggers the relay to turn off the detectors if the count rate is too high.



Figure 3-13 The APD detector

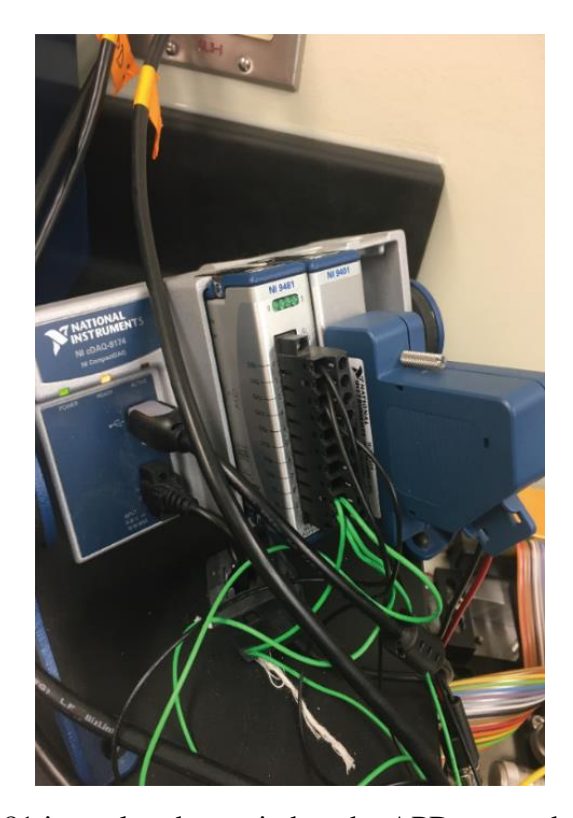


Figure 3-14 The NI 9481 is a relay that switches the APDs on and off.

4 Applications and Verification

4.1 Calibration

The confocal volume is calibrated using a Gaussian fit function (equation 2.15). First, various sample concentrations are studied to determine the optimal values for experiments. We decided to use Rhodamine 6G with a known concentration because it is popular in the calibration of FCS and has a published diffusion coefficient of 2.8 x 10⁻⁶ cm²s⁻¹. The count rate and concentration are compared in the graph shown in table 4-1. As the concentration increases, the count rate increases. Figure 4-1 was predicted to be theoretically linear; however, it has a nonlinear trend. This nonlinear trend is due to the afterpulsing from our APD detector. Since the APD deadtime is 35 ns, and the software sampling rate is at 25 ns, afterpulsing will influence our data. This afterpulsing trend was

observed in Schuab software [109, 113], and was corrected using a correction factor (equation 2.18). However, the correction factor is not applied in our correlator and, therefore, must be accounted for in the measurements for now.

FCS curves at different concentrations with coverslips

	*
1 nM	94.583 Hz
10 nM	262.23 Hz
100 nM	31,328.5 Hz
1 μΜ	632,351 Hz
10 μΜ	4.15037⋅ 10 ⁶ Hz

Laser at 60 µW, pinhole at 50 µm, 10 µL volume RG6

Table 4-1 Comparison of the count rate to the concentration.

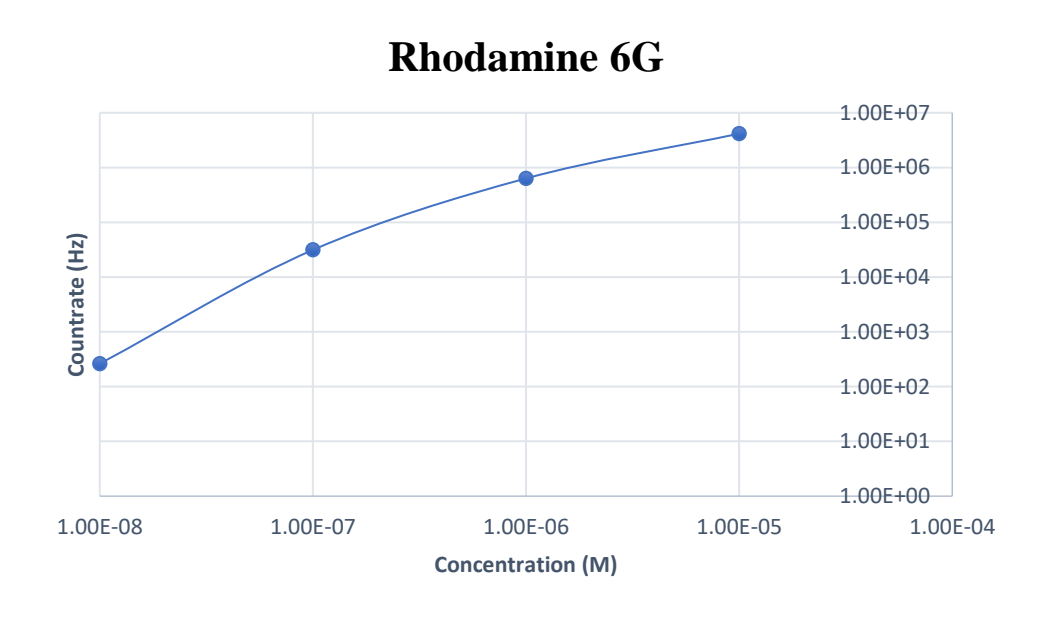


Figure 4-1 The nonlinear trend in our count rate is shown. We conclude that the trend is due to the afterpulsing of the APD detector. This afterpulsing will be corrected in the future.

4.2 Photobleaching

Photobleaching is observed in the presence of RG6 dye on coverslips. The data was fit to a linear fitting function resulting in a $R^2 = 0.8391$. However, photobleaching was reduced in the presence of custom-made slides due to the increase in surface area. Figure 4-2 shows the rate of photobleaching of 100 nM RG6 with an excitation power of ≈ 1 mW.

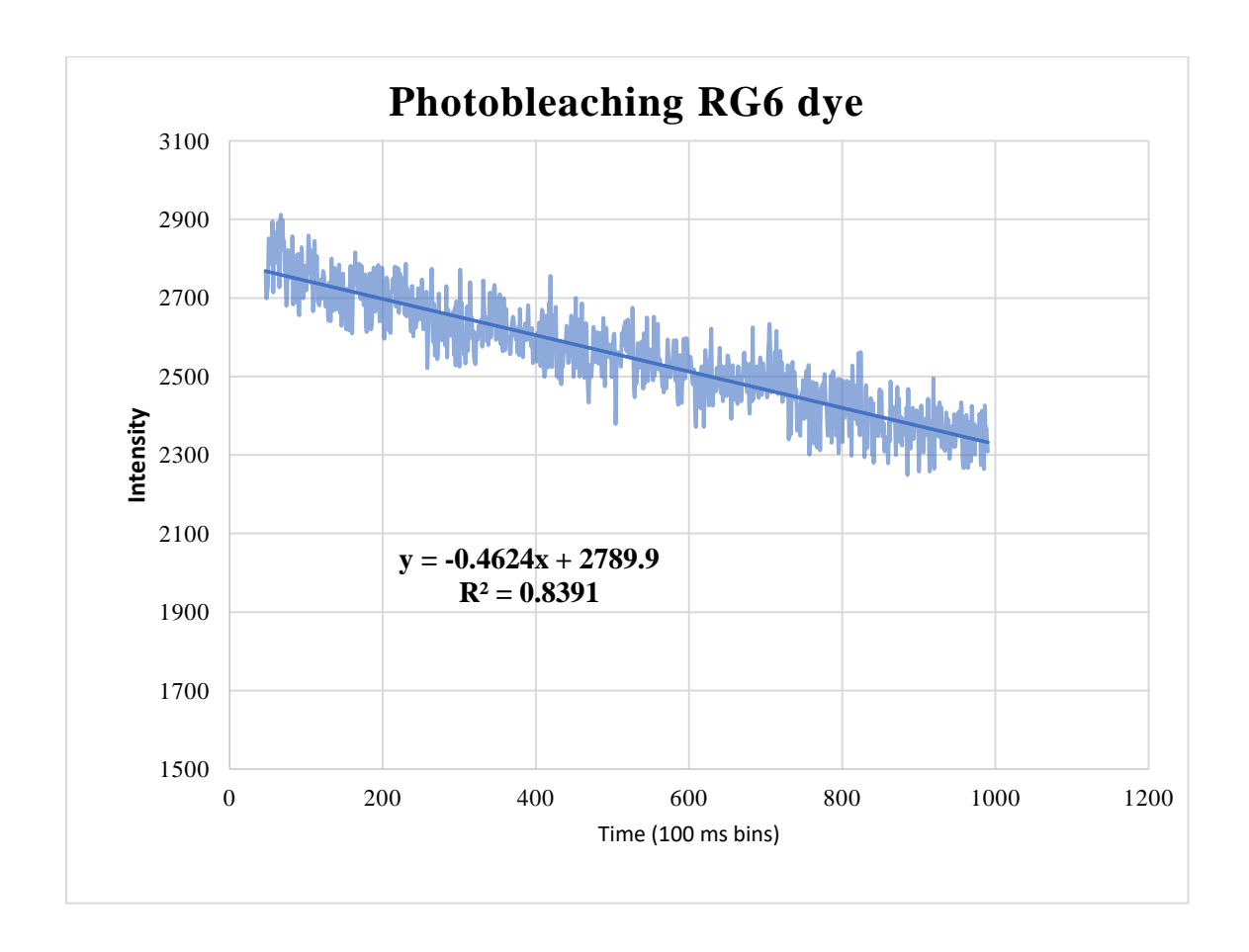


Figure 4-2 Photobleaching of the dye was observed in experiments that used coverslips. This is due to the sample being restricted to a small surface area. The samples that were made with slides, bleached less, and were more stable.

4.3 Concentration Selection

Serial 1:10 dilutions of stock 100 µM RG6 were made to determine the best dye concentrations to use for experiments. Table 4-2 shows that 100 nM was the best concentration to calibrate the instrument. Higher concentrations of the sample led to software overflow and detector saturation. The recommended dye concentrations are roughly 100 nM. 100 nM concentration gave the best results by providing a reasonable count rate while not being too concentrated where detector saturation can occur. Also, it decreases the number of software overflows that could transpire. At concentrations of 1 nM and 10 nM, the count rate was too low and allowed detector artifacts and background noise to dominate the signal.

Laser Power vs. CPS					
Conc.	1 nM	10 nM	100 nM	1µM	10 μΜ
10 μW	105.4	102.7	10,756	97,888	1.18×10^{6}
50 μW	98	93.7	10,462	356,049	3.42×10^{6}
100 μW	106	110	14,360	710,535	5×10^{6}
200 μW	99	176	32,821.6	1.33×10^{6}	Not tested

Table 4-2 The laser power was compared to the intensity values. CPS highlighted in orange represent count rates that caused software overflows for the dual correlator. 100 nM was determined to be a good concentration to start calibrations.

4.4 Correlator Test

Comparisons of measurements were performed between the multi tau correlator and the dual correlator to see if there is any variance between the accuracies of the diffusion measurements and confocal volume.

The V_{eff} was calculated from equation 2.5. Though the detection width (ω_{xy}) varied, we selected 396 nm for the ω_{xy} to calibrate our system. We found this focal size to return consistent diffusion coefficients for both RG6 and bead samples. The diffusion coefficient for the dual correlator and multi tau were 2.1 and 2.80 x 10^{-6} cm²s⁻¹, respectively. Diffusion times were 186 and 135 μ s for the dual correlator and multi tau correlator, respectively. The V_{eff} was difficult to narrow down with values of 0.002 and 0.007 fl for the dual and multi tau correlators, respectively.

We believe this is from the Poisson noise and afterpulsing that can enhance fluctuations to our signal causing complications in fitting the data. In addition, dye aggregation can be another reason there are spikes throughout the curve. [114, 46] The dual correlator gave a smoother look to the curve, which provides a better fit to the data. This smoothness is due to the larger bins that the dual correlator uses. In the future, we plan to optimize the system to decrease the amount of noise, which will permit lower concentrations of samples to be studied.

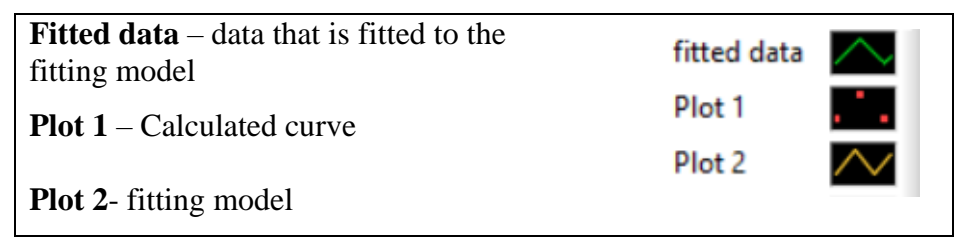


Figure 4-3 Information about figure legend

4.4.1 Rhodamine 6G Comparison

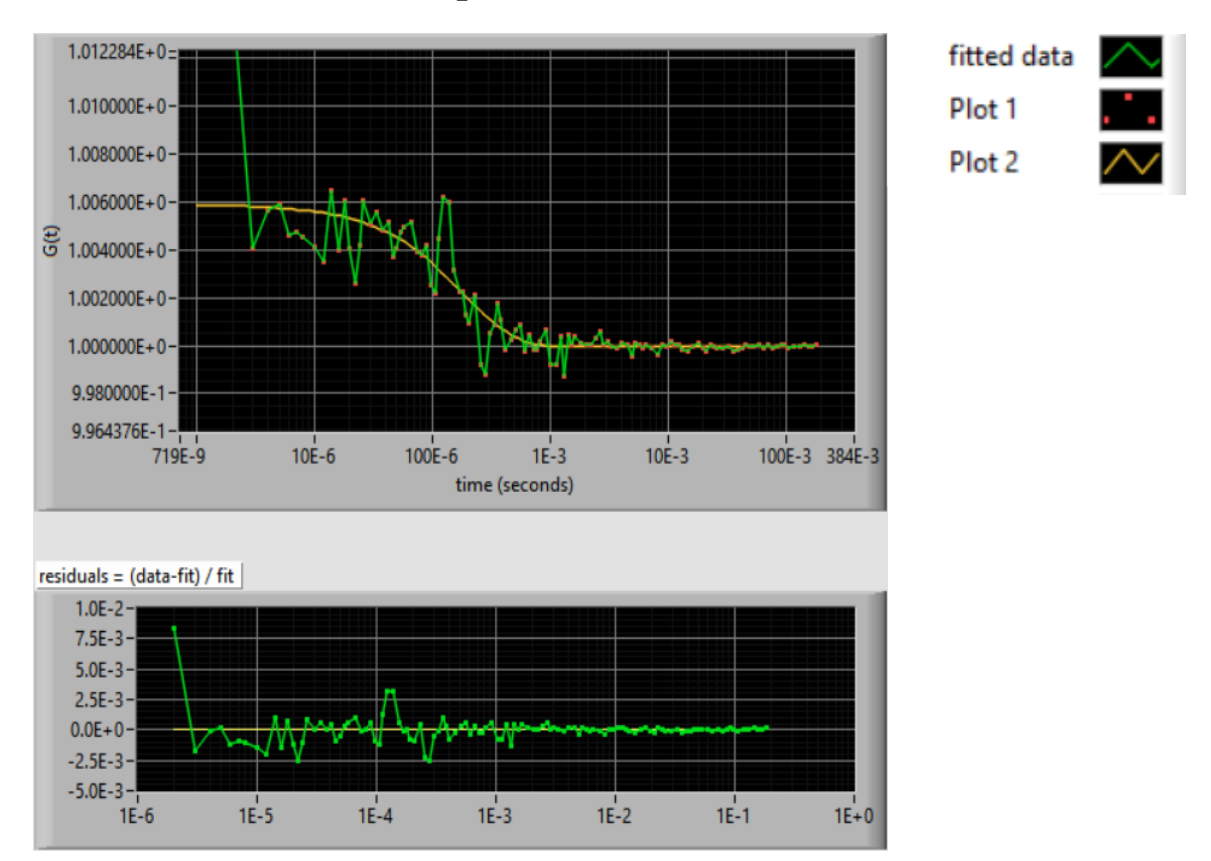


Figure 4-4 RG6 dye on the dual correlator. Residuals show that the data fits better compared to the multi tau correlator. The first data point is an indication of detectors afterpulsing.

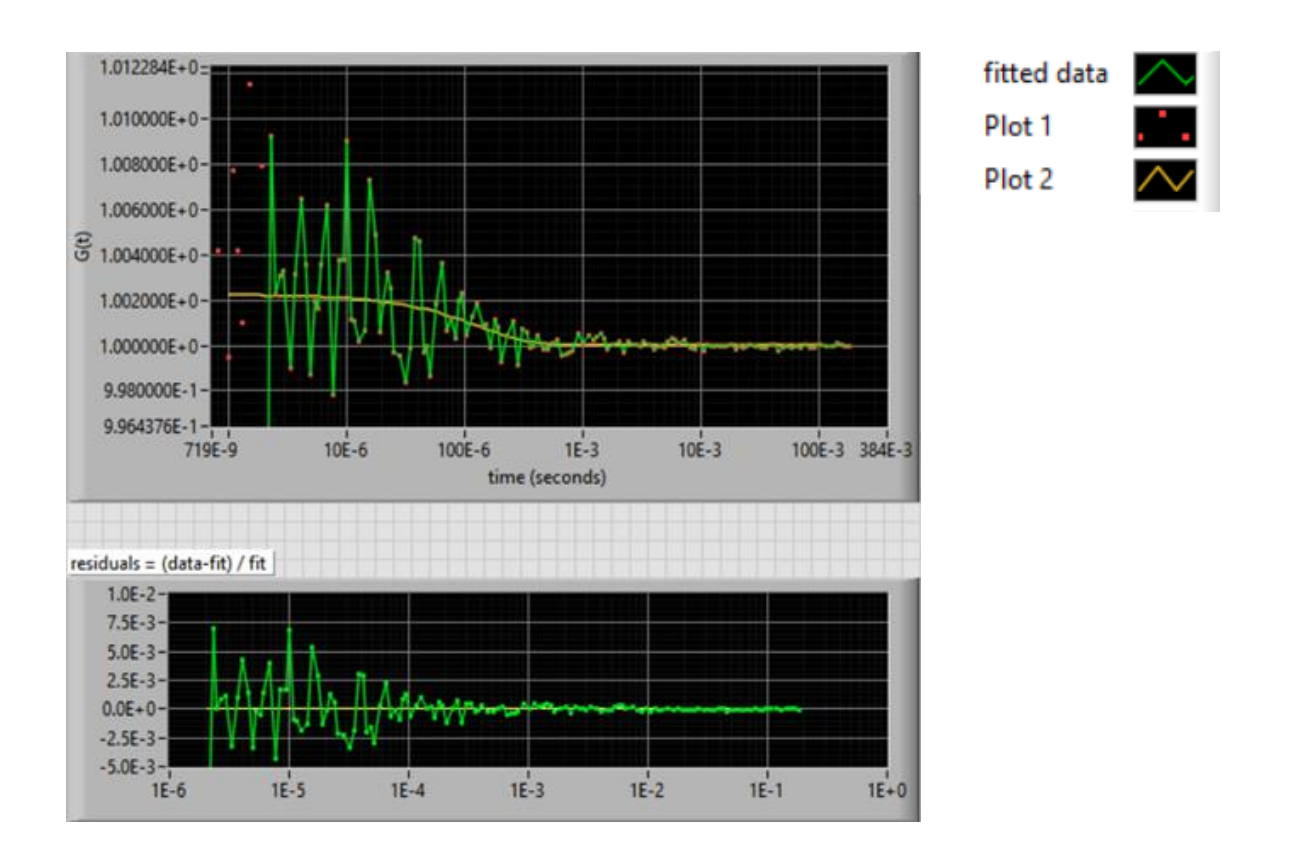


Figure 4-5 The multi tau correlator results show that the data is noisier compared to the dual correlator but gets smoother in the millisecond range. Spikes could occur from Poisson noise or aggregation of the dye.

4.4.2 TetraSpeck beads

Next, TetraSpeck beads were used to observed slower molecules to determine whether or not our software can estimate the correct hydrodynamic radius (equation 2.4). From the fits, we determined that the beads diffused at a rate of 4.3 and 4.7 x 10^{-8} cm²s⁻¹ for the multi tau and the dual correlator, respectively. We were able to calculate a hydrodynamic radius of approximately 50 nm. This is approximately the size we would expect from 100 nm diameter beads. Both correlators were able to produce smooth curves with the bead samples. This smoothness is due to the brightness of the TetraSpeck beads. Therefore, it can overcome noise from our system.

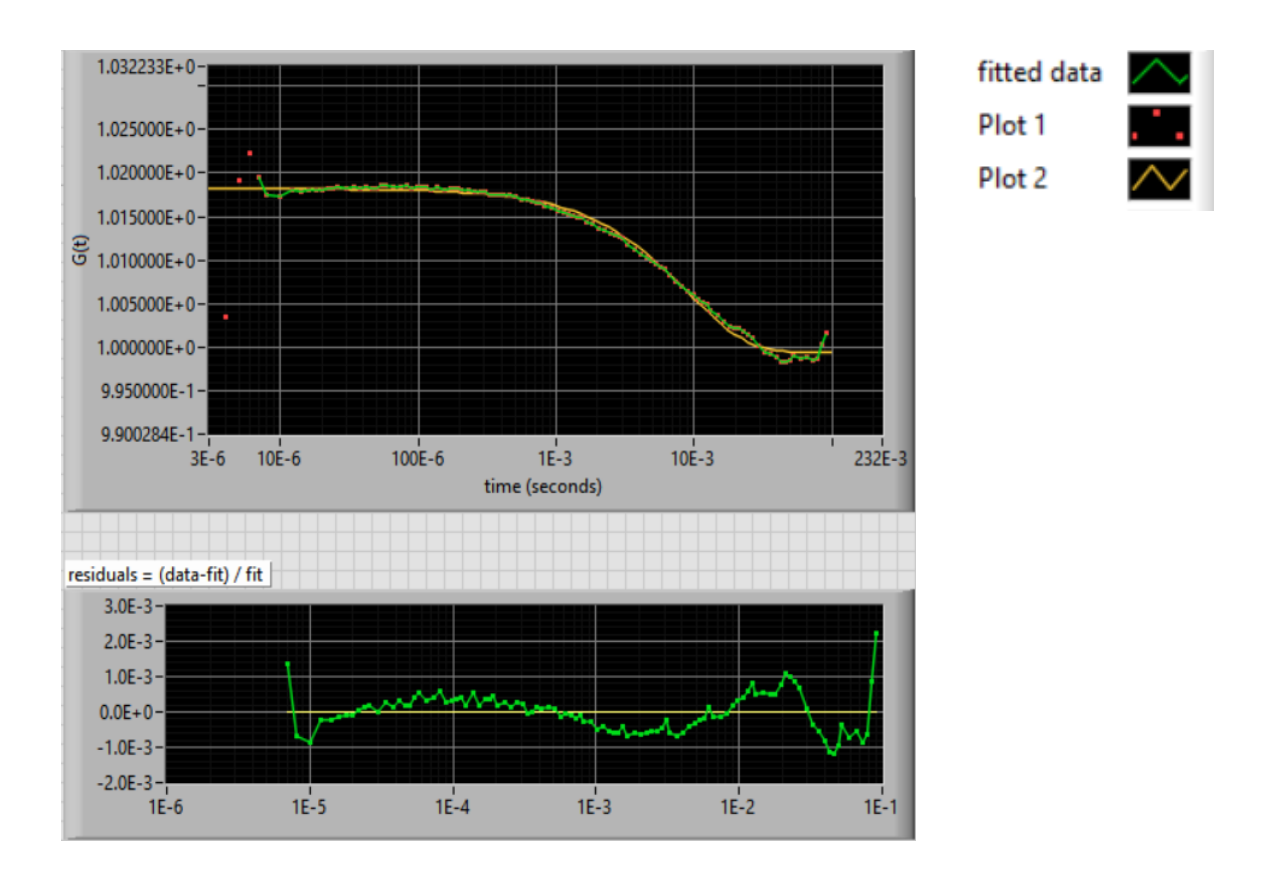


Figure 4-6 Dual Correlator with TetraSpeck beads

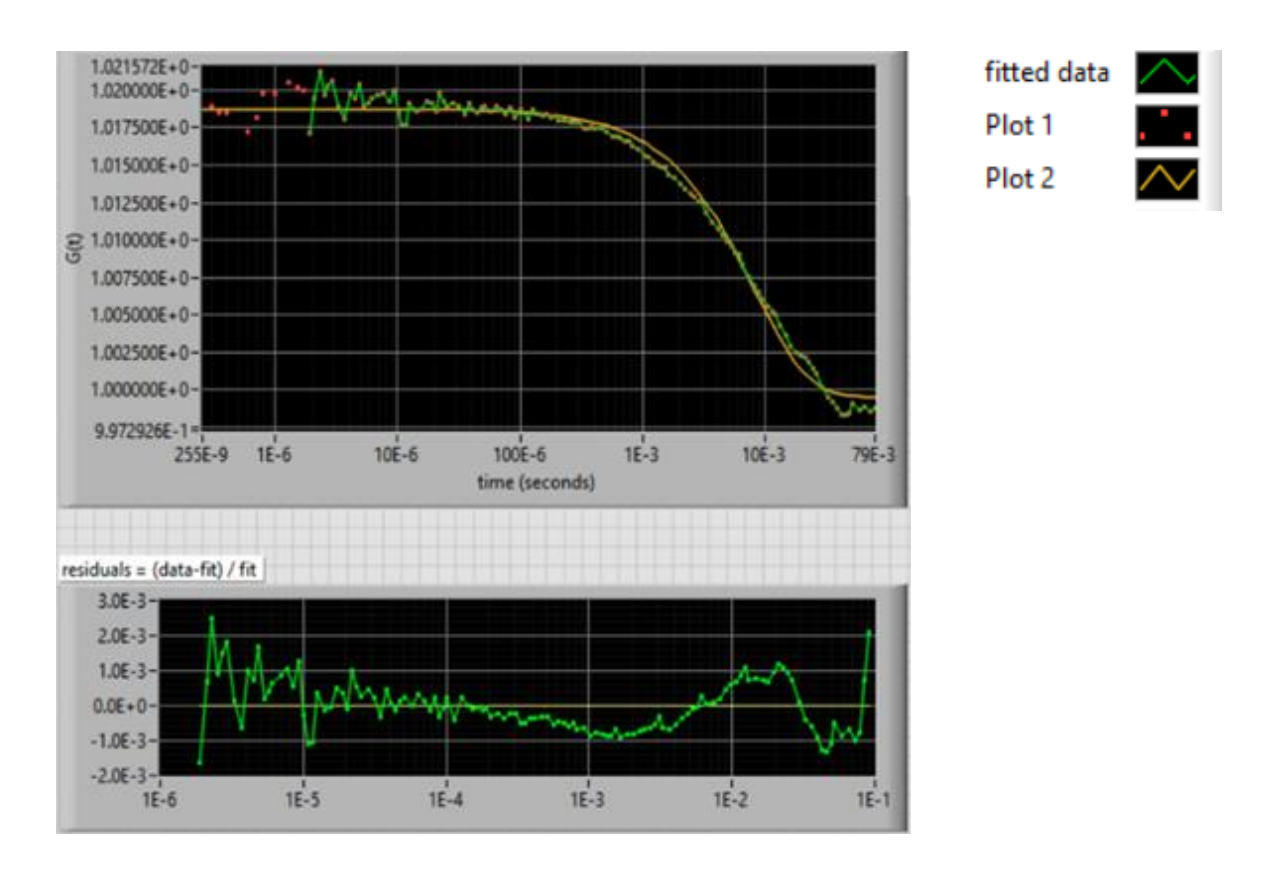


Figure 4-7 Multi tau correlator with TetraSpeck beads. Results are like the dual correlator.

In conclusion, we were able to calibrate the instrument using RG6 and a diffusion coefficient of $2.80 \times 10^{-6} \, \mathrm{cm^2 s^{-1}}$. The dual correlator and multi correlator both worked efficiently to retrieve the diffusion coefficients of the free dye and the 100 nm fluorescence beads. While the multi tau correlator struggled in the microsecond region with noise, the dual correlator was able to overcome the noise by using bigger bin sizes of $1\mu s$.

It may be necessary to use the dual correlator for volume calibration to calculate the size more efficiently. We suggest using the dual correlator for faster and smaller molecules such as free dye while using the multi tau for larger biological molecules, such as the ribosome. A limitation of the dual correlator is that it has trouble with handling

count rates over 100 kHz (Table 4-3). We would suggest using the multi tau correlator for high count rates or lower the laser power to decrease the count rate.

4.5 Acquisition Time

The SNR was compared over time by taking 5, 10, 30, and 60-second measurements. We found that the SNR improves as the measurement time increases, as Koppel concluded in his data [115]. A sustainable count rate must be maintained throughout the experiment to ensure that the FCS curve has an excellent SNR and to maintain stability in the dual correlator data as the multi tau correlator must be stable to merge the linear correlator correctly. Over time, the fits to the FCS curves improved- this is determined from the x^2 values observed in table 4-3. One-minute scans were determined to work in most cases as long as the count rate is high. For a lower count rate of <20kHz, acquisition times must be longer in order to build up statistics.

Acquisition Time (s)	$ au_d$ (s)	x^2	Amplitude	x^2	Diffusion Co $10^{-6} cm^2 \cdot s^{-1}$	ω _{xy} (nm)
5	1.15e-5	1.35 e-5	1.07e-2	5.34e-3	34.13	396
10	1.72e-5	6.13e-5	4.20e-3	5.31e-5	2.28	396
30	1.98e-4	3.78e-5	6.17e-3	4.0e-4	1.97	396
60	1.86e-4	2.89e-5	5.95e-3	3.18e-4	2.10	396

Table 4-3 Orange box represents the outlier in the data. The table shows how x^2 values get better as the measurement time increases. Indicating that the SNR gets better over time.

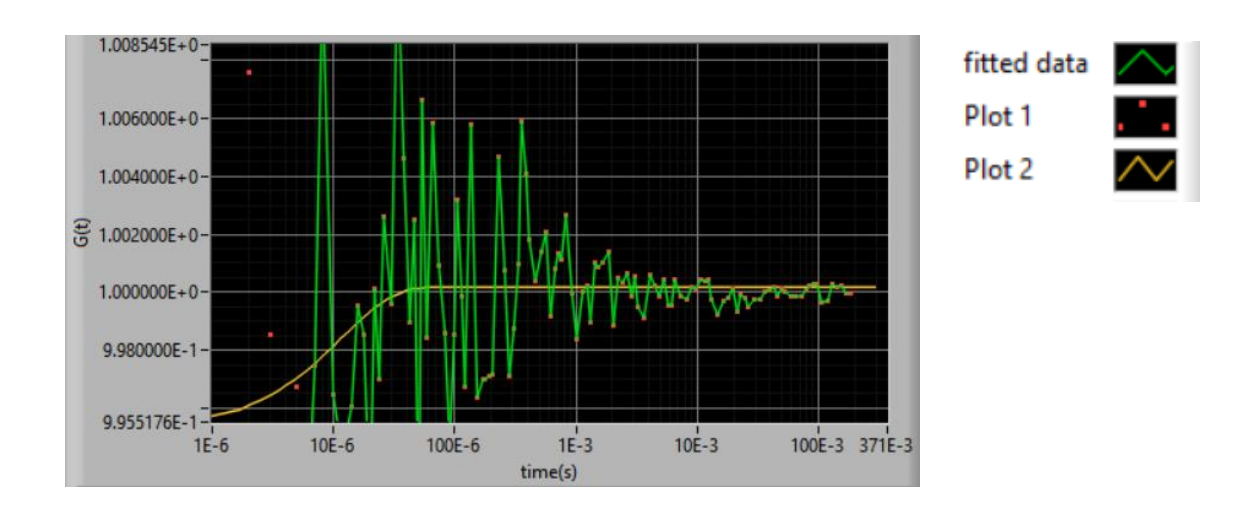


Figure 4-8 5 second measurements

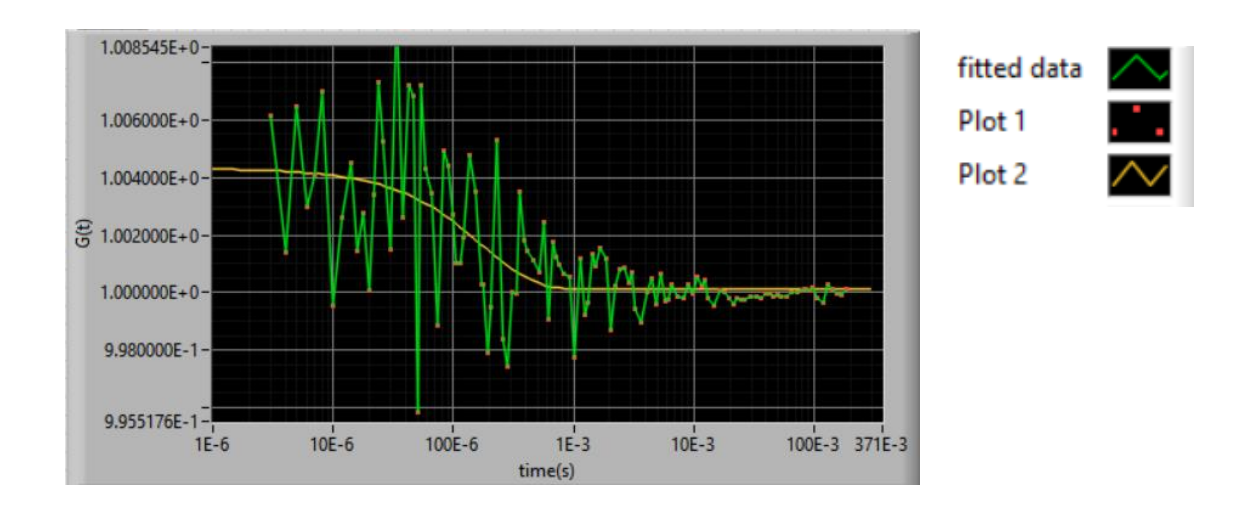


Figure 4-9 10 second measurements

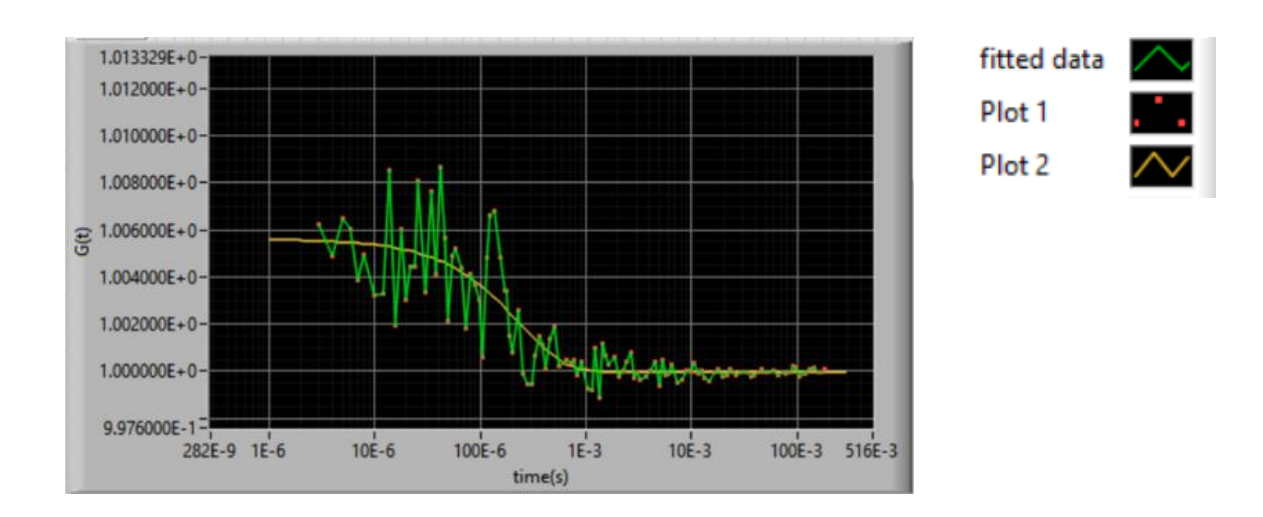


Figure 4-10 30 second measurement

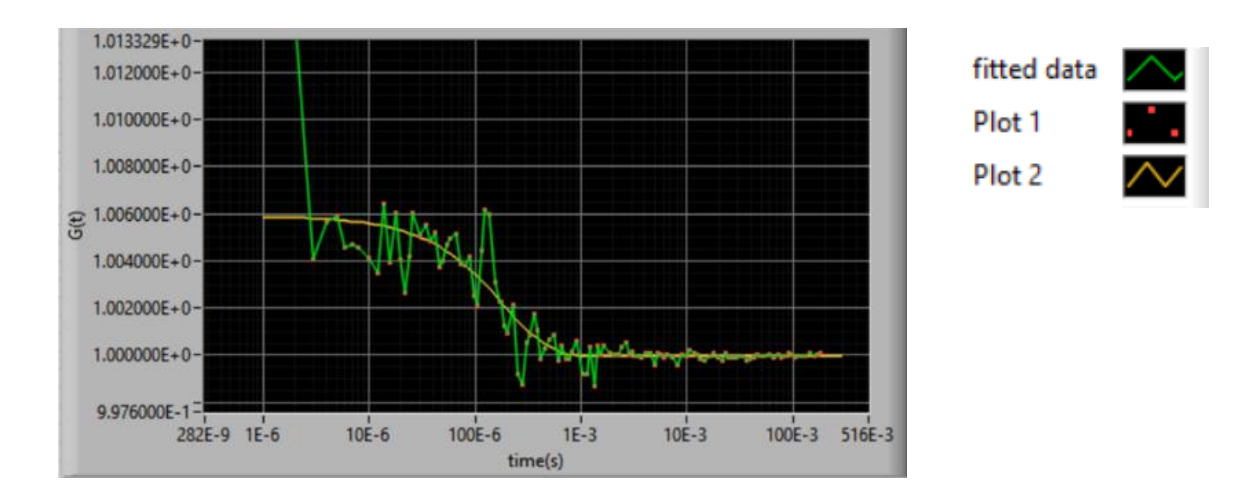


Figure 4-11 60 second measurement

However, the acquisition results will rely on the brightness of the dye. In the case of the bright TetraSpeck beads, the curve maintains good SNR throughout the measurement, and an FCS curve appeared immediately. We discovered that we must maintain the signal between 30kHz and 100kHz, depending on the brightness and quantum yield of the dye.

4.6 Applications to Biological Molecules

4.6.1 27 base m91 DNA

Since the diffusion coefficient of the DNA depends on the length [116], we were able to theorize that a 27 base length DNA should diffuse on the same magnitude of the RG6 dye. Diffusions coefficients were obtained from the dual correlator and the multi correlator at $2.3 \times 10^{-6} \, \text{cm}^2 \text{s}^{-1}$ and $2.4 \times 10^{-6} \, \text{cm}^2 \text{s}^{-1}$, respectively.

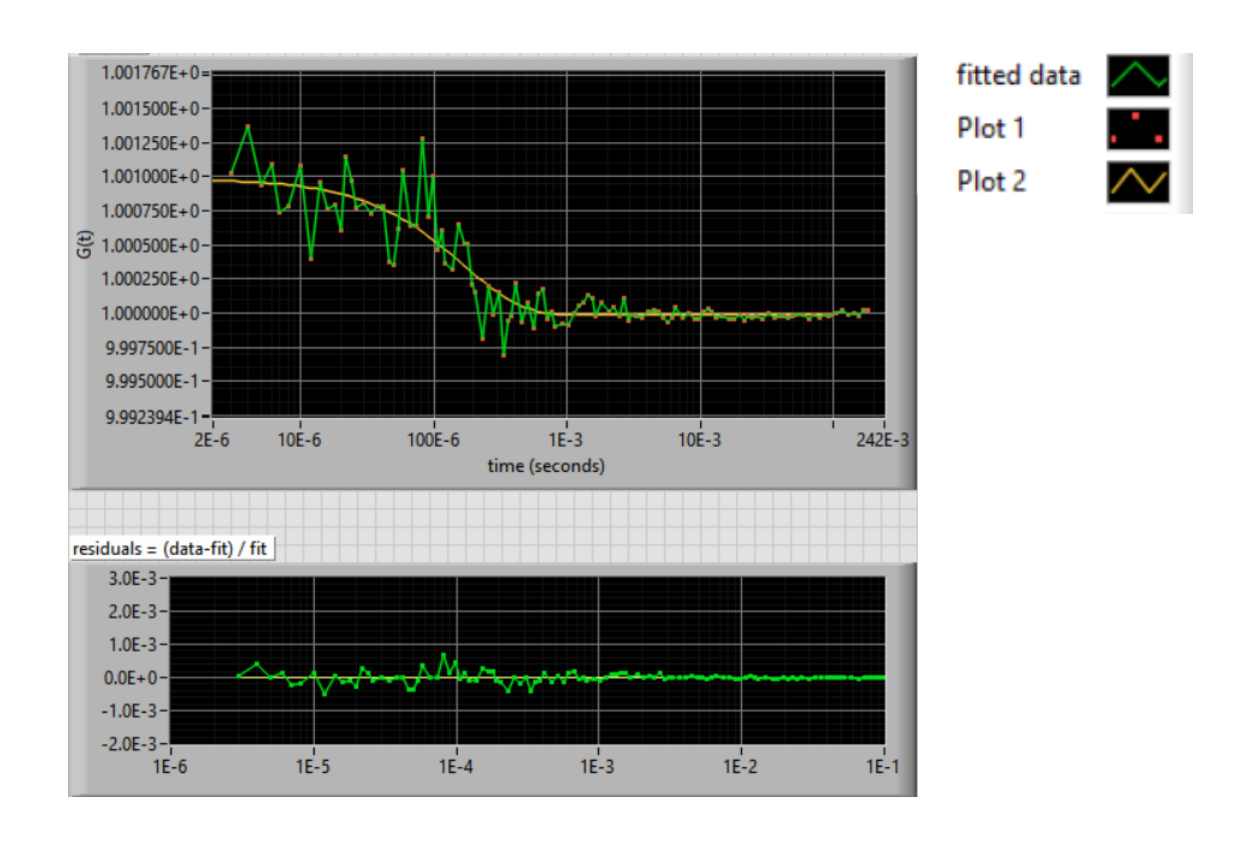


Figure 4-12 Dual correlator results from the DNA

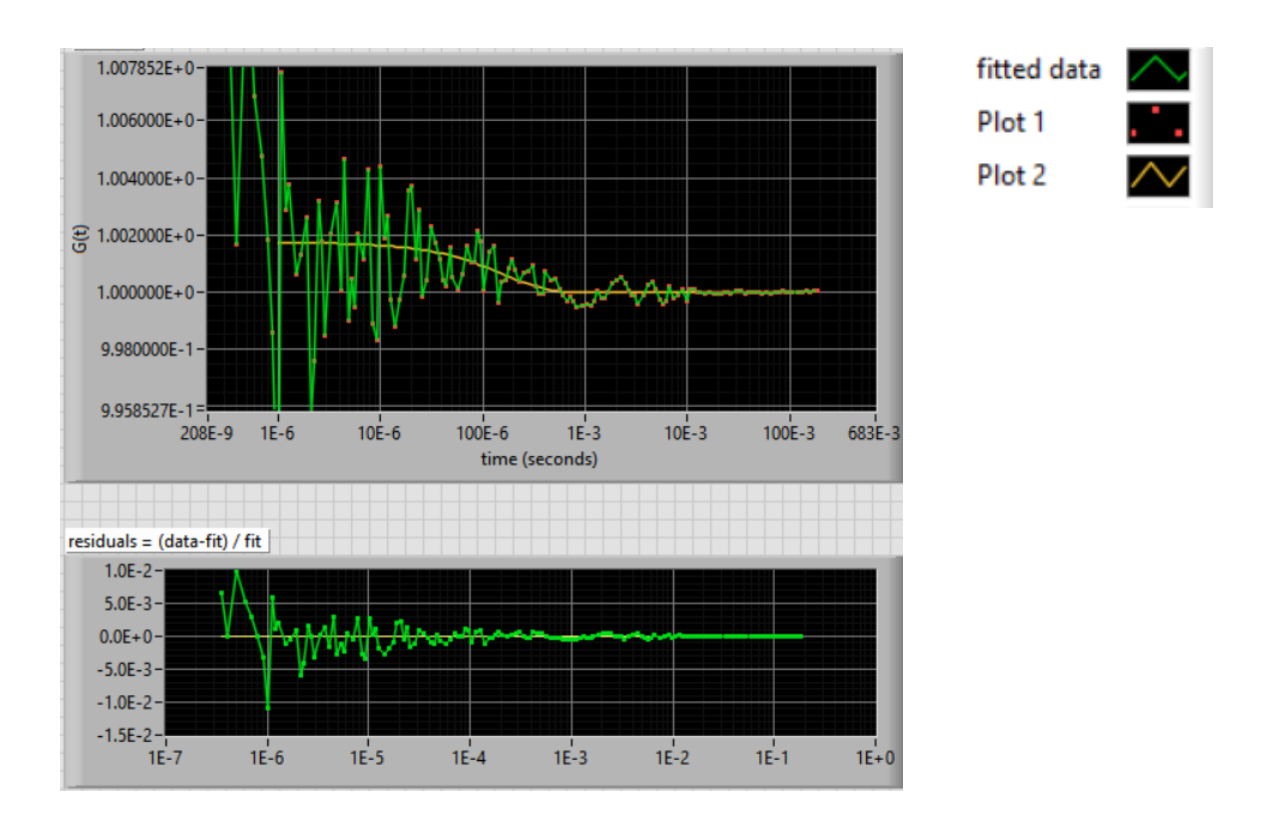


Figure 4-13 Multi tau correlator results of the DNA.

4.6.2 Ribosome, mRNA, with labeled Alexa 546 DNA

Next, we investigated the diffusion of the 70S ribosome in the presence of m291 RNA, and Alexa 546 labeled m91 DNA. Because the ribosome is large, \approx 20 nm, longer measurement times are required for the experiment. The acquisition time was set to an arbitrary time of 1000 seconds. From our graph, we determined that there is a possible two-component fit, indicating that there is some inhomogeneity in the data. We used the Quick Fit software [117], which provided advanced fit functions to apply to our system.

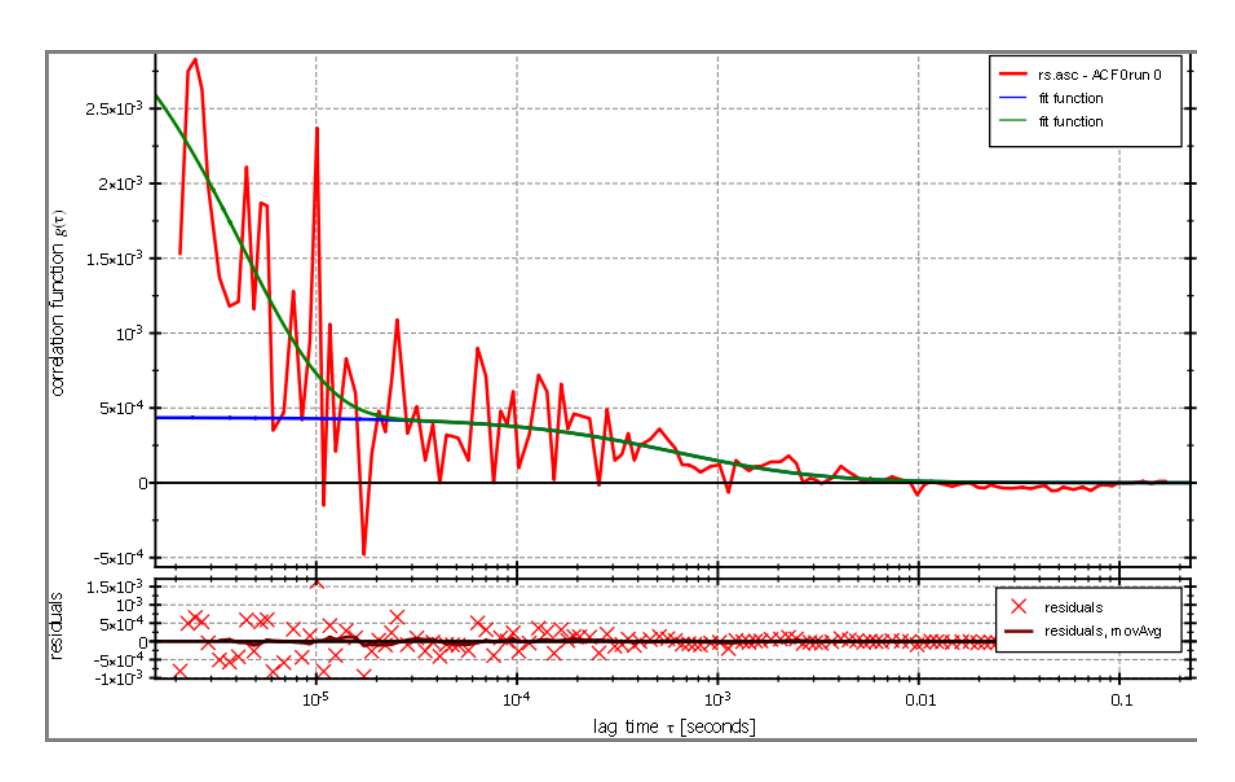


Figure 4-14 Quick Fit results of the labeled DNA, mRNA, and ribosome sample. Two components were able to be fit from our curve.

Upon fitting the data, we were able to get a double fit and observed that there is a faster and slower component. The slower diffusion coefficient was determined to be ≈ 4.1 x 10^{-7} cm²s⁻¹. We could speculate that the faster component is possibly free labeled DNA, while the slower component is the ribosome. However, we must keep in mind that the dye triplet state could be the fast component, and the slow component could be some fluctuation noise.

In the past, diffusion coefficients were obtained at 1.7, 1.9, and roughly 2.1 x 10⁻⁷ cm²s⁻¹ for 10 mM Mg²⁺ and at temperatures between 0°C and about 40°C. Gabler investigated the diffusion of the 70S, 50S, and 30S ribosomes using laser spectroscopy. Results from Gabler agreed with results that were reported by Koppel [118, 119]. Though we are on the same order of magnitude in diffusion time, more data must be

taken to determine if we see ribosome diffusion in the $100 \mu s$ region or if this data is dominated by noise. In the future, we will need to repeat the experiment in order to determine our hypothesis.

4.7 Summary

In conclusion, we have proven that our FCS instrument can calculate molecules of different sizes with the option of selecting between a dual correlator or multi tau correlator. In continuing it is imperative to know your sample as results can be misleading if the user is not aware of what diffusion times they should observe. It is best to:

- Have an idea of the hydrodynamic size of the molecules and be aware of the conformational state of your sample. Different conformations can change the length of your sample, therefore, affecting the hydrodynamic radius.
- 2. Investigate published diffusion coefficients and diffusion times
- Calibrate the instrument before each experiment to ensure proper volume size for calculation.

In the future, we will continue our optimization of the system to increase the SNR. We also hope to increase the sensitivity of the system so that we can use lower concentrations of the sample to perform more single molecule experiments.

5 Outlook

Single molecule techniques prove essential in studying ribosome dynamics by offering advantages over bulk techniques. In keeping, this is just the beginning of studying ribosome dynamics using single molecule techniques, and there are still areas to explore and confirm. The goal of this study was to assemble a Fluorescence Correlation Spectroscopy (FCS) setup and design a flexible correlator to allow the user to study a variety of samples on different timescales. The system was designed with a confocal microscope to eliminate the out of focus noise that can overwhelm samples. The user can select two types of correlators from the software: dual correlator or a multi tau correlator. Each correlator has an advantage. It was discovered that the dual correlator works well with fast samples because of the large bins sizes that help decrease the Poisson noise that

enters the system. While the multi tau correlator can calculate correlations over several time scales using a high-speed binning technique.

5.1 Corrections in the system

In the future, several corrections can take place. 1) It can be beneficial to optimize the alignment of the confocal set up in order to gain sensitivity to lower concentrated samples. Although brighter dyes will help overcome the noise, it would be helpful to be able to detect lower concentrations of dyes, i.e., Rhodamine or Cy3, for single molecule experiments. Recalibration of the system could help with increasing the resolution. 2) A beam splitter can be used to cross-correlate the signal, or a correction factor (equation 2.18) can be added to the software to decrease the effects of afterpulsing.

5.2 Optimizations in the software

In continuing, an extension of the dual correlator to include Fluorescence Cross-Correlation Spectroscopy could be considered. Also, we will like to combine FCS with FRET to look at if there is a possibility that the diffusion coefficients can change based on the different FRET states of a sample. We plan to continue the FCS experiments on the ribosome in the presence of DNA and RNA to verify the results that we received in chapter 4. Other binding experiments will be looked at again to see if we get successful results from RNA/DNA samples and proteins S6/L9.

5.3 Developments in the system

Several ways to optimize single molecule experiments in the future are (a) expanding the number of samples to study and (b) combining techniques. The ribosome is very

complex; therefore, it would be interesting to investigate multiple motions that could transpire. New optimizations of the instrument could include expanding instrumentation to allow more detectors, faster time resolution, among other techniques. Optimizations can also include combinations of instruments that will allow observation of the molecules under the same environment and conditions, such as FCS-FRET. FCS-FRET could allow us to monitor distance changes with smFRET, while simultaneously understanding how fast the proteins bind or diffuse with FCS. [120]

References

- [1] J. R. Williamson, M. T. Sykes and Z. Shajani, "Assembly of Bacterial Ribosomes," *Annu. Rev. Biochem.*, pp. 501-526, 2011.
- [2] I. J. K. H. Y. S. Tinoco, "Frameshifting," Biopolymers, pp. 1147-1166, 2013.
- [3] P. Qin, D. Yu, X. Zuo and P. V. Cornish, "Structured mRNA induce ribosome into a hyper-rotated state," *EMBO reports*, pp. 185-190, 2014.
- [4] D. N. Ermolenko, P. C. Spiegel, Z. K. Majumdar, R. P. Hickerson, R. M. Clegg and H. F. Noller, "The antibiotic viomycin traps the ribosome in an intermediate state of translocation," *Nature Structural & Molecular Biology*, vol. 14, no. 6, pp. 493-497, 2007.
- [5] P. B. Moore and T. A. Steitz, "The ribosome revealed," *TRENDS in Biochemical Sciences*, pp. 281-282, 2005.
- [6] A. Antoun, M. Y. Pavlov, M. Lovmar and M. Ehrenberg, "How initiation factors tune the rate of initiation of protein synthesis in bacteria," *The EMBO Journal*, pp.

- 2539-2550, 2006.
- [7] V. Ramakrishnan, "Ribosome Structure and the Mechanism of Translation," *Cell*, pp. 557-572, 2002.
- [8] S. H. Sternberg, J. Fei, N. Prywes, K. A. McGrath and R. Gonzalez Jr, "Translation factors direct intrinsic ribosome dynamics during translation termination and ribosome recycling," *Nature Structural & Molecular Biology*, pp. 861-869, 2009.
- [9] J. Frank, J. Zhu, P. Penczek, Y. Li, S. Srivastava, A. Verschoor, M. Radermacher, R. Grassucci, R. Lata and R. Agrawal, "A model of protein synthesis based on cryo-electron microscopy of the E. coli ribosome.," *Nature*, vol. 376, pp. 441-444, 1995.
- [10] A. Tyczewsha and K. Bakowska-Zywicka, "The strucutre of the ribosome-short history," *Biotechnologia*, pp. 14-23, 2009.
- [11] J. Frank and R. K. Agrawal, "A ratchet-like inter-subunit reorganization of the ribosome during translocation," *Nature*, pp. 318-322, 2000.
- [12] C. M. Kaiser and I. Tinoco Jr., "Probing the Mechanisms of Translation with Force," *Chemical Reviews*, pp. 3266-3280, 2014.
- [13] P. V. Cornish and T. Ha, "A Survey of Single-Molecule Techniques in Chemical Biology," *ACS Chemical Biology*, pp. 53-61, 2007.
- [14] C. Gell, D. Brockwell and A. Smith, Handbook of Single Molecule Fluorescence Spectroscopy, New York: Oxford University Press, 2006.
- [15] T. Ha, V. Sandoghdar and M. Orrit, "Single-molecule optical spectroscopy," *Chem Soc Rev*, pp. 973-976, 2014.
- [16] Z. Norman, B. Shebl and P. V. Cornish, "Ribosome structure and dynamics by smFRET microscopy," *Riboswitches*.
- [17] T. Ha, "Single-Molecule Fluorescence Resonance Energy Transfer," *Methods*, pp. 78-86, 2001.
- [18] C. Y. I. D. B. C. Moffitt JR, "Differential detection of dual traps improves the spatial resolution of optical tweezers.," *Proc Natl Acad Sci*, pp. 9006-9011, 2006.
- [19] T. Masuda, A. N. Petrov, R. Iizuka, T. Funatsu, J. D. Pulisi and S. Uemura, "Initiation factor 2, tRNA, and 50S subunits cooperatively stablize mRNAs on the ribosome during initation," *PNAS*, pp. 4881-4885, 2012.
- [20] J. Wang, K. Caban and R. L. Gonzalez Jr., "Ribosomal Initiation Complex-Driven

- Changes in the Stability and Dynamics of Initiation Factor 2 Regulate the Fidelity of Translation Initiation," *J Mol Biology*, pp. 1819-1834, 2015.
- [21] C. Ling and D. N. Ermolenko, "Initiation factor 2 stabilizes the ribosome in a semirotated conformation.," *Proceedings of the National Academy of Sciences of the United States of America*, vol. 112, no. 52, pp. 15874-15879, 2015.
- [22] M. M. Elvekrog and R. I. Gonzalez Jr., "Conformational selection of translation initiation factor 3 signals proper substrate selection," *Nature Structural & Molecular Biology*, pp. 628-635, 2013.
- [23] D. D. MacDougall and R. L. Gonzalez, Jr., "Translation Initiation Factor 3 Regulates Switching between Different Modes of Ribosomal Subunit Joining," *Journal of Molecular Biology*, pp. 1801-1818, 2014.
- [24] K. Caban, M. Y. Pavlov, M. Ehrenberg and R. L. Gonzalez, "A conformational switch in initiation factor 2 controls the fidelity of translation initiation in bacteria," *Nature Communications*, vol. 8, no. 1, p. 1475, 2017.
- [25] P. V. Cornish, D. N. Ermolenko, H. F. Noller, T. . Ha and T. . Ha, "Spontaneous intersubunit rotation in single ribosomes.," *Molecular Cell*, vol. 30, no. 5, pp. 578-588, 2008.
- [26] T. Ha, H. F. Noller, D. N. Ermolenko and P. V. Cornish, "Spontaneous Intersubunit Rotation in Single Ribosomes," *Mol. Cell.*, pp. 578-588, 2008.
- [27] P. V. Cornish, D. N. Ermolenko, D. W. Staple, L. . Hoang, R. P. Hickerson, H. F. Noller, T. . Ha and T. . Ha, "Following movement of the L1 stalk between three functional states in single ribosomes," *Proceedings of the National Academy of Sciences of the United States of America*, vol. 106, no. 8, pp. 2571-2576, 2009.
- [28] D. N. Ermolenko, Z. K. Majumdar, R. P. Hickerson, P. C. Spiegel, R. M. Clegg and H. F. Noller, "Observation of Intersubunit Movement of the Ribosome in Solution Using FRET," *Journal of Molecular Biology*, vol. 370, no. 3, pp. 530-540, 2007.
- [29] E. . Salsi, E. . Farah, J. . Dann and D. N. Ermolenko, "Following movement of domain IV of elongation factor G during ribosomal translocation," *Proceedings of* the National Academy of Sciences of the United States of America, vol. 111, no. 42, pp. 15060-15065, 2014.
- [30] M. R. Wasserman, J. L. Alejo, R. B. Altman and S. C. Blanchard, "Multiperspective smFRET reveals rate-determining late intermediates of ribosomal translocation," *Nature Structural & Molecular Biology*, vol. 23, no. 4, pp. 333-341, 2016.

- [31] R. A. Marshall, M. Dorywalska and J. D. Puglisi, "Irreversible chemical steps control intersubunit dynamics during translation," *PNAS*, pp. 15364-15369, 2008.
- [32] J. Fei, P. Kosuri, D. MacDougall and R. L. Gonzalez Jr., "Coupling of Ribosomal L1 Stalk and tRNA Dynamics during Translation Elongation," *Molcular Cell*, pp. 348-359, 2008.
- [33] D. N. Ermolenko and H. F. Noller, "mRNA translocation occurs during the second step of ribosomal intersubunit rotation," *Nature Structural & Molecular Biology*, vol. 18, no. 4, pp. 457-462, 2011.
- [34] J. Chen, A. Petrov, A. Tsai, S. E. O'Leary and J. D. Puglisi, "Coordinated conformational and compositional dynamics drive ribosome translocation.," *Nature Structural & Molecular Biology*, vol. 20, no. 6, pp. 718-727, 2013.
- [35] H. Sharma, S. Adio, T. Senyushkina, R. Belardinello, F. Peske and M. Rodnina, "Kinetics of Spontaneous and EF-G-Accelerated Rotation of Ribosomal Subunits," *Cell Rep.*, pp. 2187-2196, 2016.
- [36] S. . Adio, T. . Senyushkina, F. . Peske, N. . Fischer, W. . Wintermeyer and M. V. Rodnina, "Fluctuations between multiple EF-G-induced chimeric tRNA states during translocation on the ribosome," *Nature Communications*, vol. 6, no. 1, pp. 7442-7442, 2015.
- [37] J. Chen, A. Coakley, M. O'Connor, A. Petrov, S. E. O'Leary, J. F. Atkins, J. F. Atkins and J. D. Puglisi, "Coupling of mRNA Structure Rearrangement to Ribosome Movement during Bypassing of Non-coding Regions," *Cell*, vol. 163, no. 5, pp. 1267-1280, 2015.
- [38] S. . Uemura, M. . Dorywalska, T.-H. . Lee, H. D. Kim, J. D. Puglisi and S. . Chu, "Peptide bond formation destabilizes Shine–Dalgarno interaction on the ribosome," *Nature*, vol. 446, no. 7134, pp. 454-457, 2007.
- [39] T. . Liu, A. . Kaplan, L. . Alexander, S. . Yan, J.-D. . Wen, L. . Lancaster, C. E. Wickersham, K. . Fredrick, H. F. Noller, I. . Tinoco and C. . Bustamante, "Direct measurement of the mechanical work during translocation by the ribosome," *eLife*, vol. 3, no., p., 2014.
- [40] C. Ling and D. N. Ermolenko, "Structural insights into ribosome translocation.," *Wiley Interdisciplinary Reviews Rna*, vol. 7, no. 5, pp. 620-636, 2016.
- [41] J.-D. Wen, L. Lancaster, C. Hodges, A.-C. Zeri, S. H. Yoshimura, H. F. Noller, C. Bustamante and I. Tinoco Jr., "Following translation by single ribosomes one codon at a time," *Nature*, pp. 598-603, 2008.

- [42] T. Liu, A. Kaplan, L. Alexander, S. Yan, J.-D. Wen, L. Lancaster, C. E. Wickersham, K. Fredrick, H. Noller, I. Tinoco Jr and C. J. Bustamate, "Direct measurement of the mechanical work during translocation by the ribosome," *eLife sciences*, pp. 1-12, 2014.
- [43] S. . Adio, H. . Sharma, T. . Senyushkina, P. . Karki, C. . Maracci, I. . Wohlgemuth, W. . Holtkamp, F. . Peske and M. V. Rodnina, "Dynamics of ribosomes and release factors during translation termination in E-coli.," *eLife*, vol. 7, no. , p. 243485, 2018.
- [44] W. Casy, A. R. Prater and P. V. Cornish, "Operative Binding of Class I Release Factors and YaeJ Stabilizes the Ribosome in the Nonrotated State," *Biochemistry*, pp. 1954-1966, 2018.
- [45] A. . Prabhakar, M. C. Capece, A. . Petrov, J. . Choi and J. D. Puglisi, "Post-termination Ribosome Intermediate Acts as the Gateway to Ribosome Recycling," *Cell Reports*, vol. 20, no. 1, pp. 161-172, 2017.
- [46] W. K. Ridgeway, D. P. Millar and J. R. Williamson, "Quantitation of ten 30S ribosomal assembly intermediates using fluorescence triple correlation spectroscopy," *Proceedings of the National Academy of Sciences of the United States of America*, vol. 109, no. 34, pp. 13614-13619, 2012.
- [47] M. A. Digman and E. Gratton, "Lessons in Fluctuations Correlation Spectroscopy," *Annual Review Phys Chem*, pp. 645-668, 2011.
- [48] P. Schwille and E. Haustein, "Fluorescence Correlation Spectroscopy: Novel Variations of an Establised Technique," *Annu. Rev. Biophys. Biomol. Struct.*, pp. 151-169, 2007.
- [49] S. A. Kim, K. G. Heinze and P. Schwille, "Fluorescence correlation spectrscopy in living cells," *Nature Methods*, pp. 963-973, 2007.
- [50] M. Nomura, S. Mizushima, B. Ballou and W. A. Held, "Assembly Mapping of 30 S Ribosomal Proteins from Escherichia coli," *The Journal of Biological Chemistry*, pp. 3103-3111, 1974.
- [51] D. Magde, E. L. Elson and W. W. Webb, *Biopolymers*, p. 29, 1974.
- [52] K. H. Nierhaus and R. Rohl, "Assembly map of the large subunt (50S) of Escherichia coli ribosomes," *Proc. Natl. Acad. Sci.*, pp. 729-733, 1982.
- [53] J. R. Williamson, D. P. Millar and W. K. Ridgeway, "Quantitation of ten 30S ribosomal assembly intermediates using fluorescence triple correlation spectroscopy," *PNAS*, pp. 1-6, 2012.

- [54] D. Magde, E. L. Elson and W. W. Webb, "Fluorescence correlation spectroscopy. I. Conceptual basis and theory," *Biopolymers*, p. 29, 1974.
- [55] D. Magde, E. L. Elson and W. W. Webb, "Fluorescence correlation spectroscopy. II. An experimental realization.," *Biopolymers*, pp. 29-61, 1974.
- [56] R. Rigler and U. Mets, "Submillisecond detection of single rhodamine molecules in water.," *J Fluoresc*, pp. 259-64, 1994.
- [57] R. Rigler, "FCS and single molecule spectroscopy," in *Single Molecule Spectroscoy* in *Chemistry*, *Physics and Biology*, Berlin, Heidelberg, Springer, 2009, pp. 7-103.
- [58] E. L. Elson, "Fluorescence Correlation Spectroscopy: Past, Present, Future," *Biophysical Journal*, vol. 101, pp. 2855-2870, 2011.
- [59] E. L. Elson, "Quick tour of fluorescence correlation spectroscoy from its inception," *Journal of Biomedical Optics*, vol. 9, pp. 857-864, 2004.
- [60] E. L. Elson, "40 Years of FCS: How It All Began," *Methods in Enzymology*, vol. 518, pp. 1-10, 2013.
- [61] P. Ferrand, J. Wenger and H. Rigneault, "Fluorescence Correlation Spectroscoy," *Methods Mol Biol*, pp. 181-95, 2011.
- [62] A. Einstein, Investigations on the Theory of the Brownian Movment, Dover Publications, INC, 1956.
- [63] S. J. Hill and L. E. Kilpatrick, "The use of fluorescence correlation spectroscopy to characterize the molecular mobility of fluorescently labelled G protein-coupled receptors," *Biochemical Society Transactions*, pp. 624-629, 2016.
- [64] P. Schwille and J. Ries, "Fluorescence correlation spectroscopy," *Bioessays*, pp. 361-368, 2012.
- [65] T. Binkert and J. Ricka, "Direct measurement of a distinct correlation function by fluorescence cross-correlation," *Phys Rev A*, vol. 39, no. 5, pp. 2646-2652, 1989.
- [66] K. Bacia, S. A. Kim, S. A. Kim and P. Schwille, "Fluorescence cross-correlation spectroscopy in living cells," *Nature Methods*, vol. 3, no. 2, pp. 83-89, 2006.
- [67] P. Schwille, F. Meyer-Almes and R. Rigler, "Dual-color fluorescence cross-correlation spectroscopy for multicomponent diffusional analysis in solution," *Biophysical Journal*, vol. 72, no. 4, pp. 1878-1886, 1997.
- [68] X. Ma, H. Y. Foo and T. Wohland, "Fluorescence Cross-Correlation Spectroscopy (FCCS) in Living Cells," *Fluorescence Spectroscopy and Microscopy: Methods*

- and Protocols, Methods in Molecular Biology, vol. 1076, pp. 557-573, 2014.
- [69] E. Sezgin and P. Schwille, "Fluorescence Techniques to Study Lipid Dynamics," *Cold Harbor Perspectives in Biology*, pp. 1-32, 2011.
- [70] P. Schwille and E. P. Petrov, "State of the Art and Novel Trends in Fluorescence Correlation Spectroscopy," *Standardization and Quality Assurance in Fluorescence Measurements*, pp. 145-197, 2008.
- [71] J. R. Lakowicz, Principles of Fluorescence Spectroscopy, Springer, 2006.
- [72] C. Gell, D. Brockwell and A. Smith, Handbook of Single Molecule Fluorescence Spectroscopy, New York: Oxford, 2006.
- [73] A. J. Pesce, C.-G. Rosen and T. L. Pasby, Fluorescence Spectroscopy: An introduction for Biology and Medicine, New York: Marcel Dekker, Inc., 1971.
- [74] G. C. Guilbault, Practical Fluorescence, New York: Marcel Dekker, 1990.
- [75] K. Bacia, E. Haustein and P. Schwille, "Fluorescence correlation spectroscopy: principles and applications.," *CSH Protocols*, vol. 2014, no. 7, pp. 709-725, 2014.
- [76] C. Eggeling, J. Widengren, R. Rigler and C. A. M. Seidel, "Photobleaching of Fluorescent Dyes under Conditions Used for Single-Molecule Detection: Evidence of Two-Step Photolysis," *Analytical Chemistry*, vol. 70, no. 13, pp. 2651-2659, 1998.
- [77] Y. Liu, T. Chen, Q. Luo and S. Zeng, "Fluorescence correlation spectroscopy considering the effect of photobleaching,", 2005. [Online]. Available: http://adsabs.harvard.edu/abs/2005spie.5630..898l. [Accessed 12 7 2019].
- [78] R. P. Kafle, M. R. Liebeskind, J. T. Bourg, E. D. White and J.-C. . Meiners, "Artifacts from photobleaching and dye-dissociation in fluorescence correlation spectroscopy," *Proceedings of SPIE*, vol. 9548, no., p., 2015.
- [79] P. P. Mondal, R. J. Gilbert and P. T. C. So, "Photobleaching reduced fluorescence correlation spectroscopy," *Applied Physics Letters*, vol. 97, no. 10, p. 103704, 2010.
- [80] J. Widengren and R. Rigler, "Mechanisms of photobleaching investigated by fluorescence correlation spectroscopy," *Bioimaging*, vol. 4, no. 3, pp. 149-157, 1996.
- [81] S. T. Hess, S. Huang, A. A. Heikal and W. W. Webb, "Biological and Chemical Applications of Fluorescence Correlation Spectroscopy: A Review," *Biochemistry*, pp. 697-705, 2002.

- [82] T. A. Laurence, S. . Ly, F. . Bourguet, N. O. Fischer and M. A. Coleman, "Fluorescence Correlation Spectroscopy at Micromolar Concentrations without Optical Nanoconfinement," *Journal of Physical Chemistry B*, vol. 118, no. 32, pp. 9662-9667, 2014.
- [83] E. Schaub, "High countrate real-time FCS using F2Cor," *Optical Express*, pp. 23543-23555, 2013.
- [84] J. . Enderlein and I. . Gregor, "Using fluorescence lifetime for discriminating detector afterpulsing in fluorescence-correlation spectroscopy," *Review of Scientific Instruments*, vol. 76, no. 3, p. 033102, 2005.
- [85] K. Steger, S. Bollmann, F. Noe and S. Dooe, "Systematic evaluation of fluorescence correlation spectroscopy data analysis on the nanosecond time scale," *Phys. Chem. Chem Phys.*, 2013.
- [86] G. Nishimura and M. Kinjo, "Dead-time distortion in fluorescence correlation measurements," *Applied Optics*, vol. 44, no. 17, pp. 3458-3467, 2005.
- [87] D. Chen, H. Ma, B. Chen, L. Jin and M. Zhao, "Afterpulsing and its correction in fluorescence correlation spectroscopy experiments," *Applied Optics*, pp. 4031-4036, 2003.
- [88] H. Vogel, R. Rigler and T. Wohland, "The Standard Deviation in Fluorescence Correlation Spectroscopy," *Biophysical Journal*, pp. 2987-2999, 2001.
- [89] S. . Saffarian and E. L. Elson, "Statistical Analysis of Fluorescence Correlation Spectroscopy: The Standard Deviation and Bias," *Biophysical Journal*, vol. 84, no. 3, pp. 2030-2042, 2003.
- [90] D. E. Koppel, "Statistical accuracy in fluorescence correlation spectroscopy," *Physical Review*, pp. 1938-1945, 1974.
- [91] H. Qian, "On the statistics of fluorescence correlation spectroscopy," *Biophysical Chemistry*, pp. 49-57, 1990.
- [92] V. Anderson, "Principle factors influencing the accuracy of FCS data, Application Note #3".
- [93] K. . Schaetzel and R. . Peters, "Noise on multiple-tau photon correlation data," , 1991. [Online]. Available: http://adsabs.harvard.edu/abs/1991spie.1430..109s. [Accessed 5 5 2019].
- [94] B. . Gamari, D. . Zhang, R. E. Buckman, P. . Milas, J. S. Denker, H. . Chen, H. . Li and L. S. Goldner, "Inexpensive hardware and software for photon statistics and

- correlation spectroscopy," arXiv: Biological Physics, vol., no., p., 2012.
- [95] K. Schatzel, M. Drewel and S. Stimac, "Photon correlation measurements at large lag times: improving statistical accuracy," *Journal of modern optics*, 1988.
- [96] K. Schatzel, "New concepts in correlator design," *Ist. Phys. Conf.*, vol. 77, no. 4, pp. 175-184, 1985.
- [97] M. S. Hromalik, K. S. Green, H. T. Philipp, M. W. Tate and S. M. Gruner, "The FPGA Pixel Array Detector," *Nuclear Instruments and Methods in Physics Research Section A: Accelerators, Spectrometers, Detectors, and Associated Equipment*, vol. 701, no. 2012, pp. 7-16, 2013.
- [98] M. J. Culbertson and D. L. Burden, "A distributed algorithm for multi-tau autocorrelation," *Review of Scientific Instruments*, 2007.
- [99] L. Yang, H. Lee, M. Wang, X. Lin, K. Hsu, Y. Chang, W. Fann and J. White, "Real-time data acquisition incorporating high-speed software correlator for single molecule spectroscopy," *Journal of Microscopy*, pp. 302-310, 2009.
- [100] G. Moscar, B. Kreith, J. Buchholz, J. W. Krieger, J. Langowski and G. Vamosi, "Mulitplexed multiplet auto- and cross- correlators on a single FPGA".
- [101] M. . Molteni and F. . Ferri, "Commercial counterboard for 10 ns software correlator for photon and fluorescence correlation spectroscopy," *Review of Scientific Instruments*, vol. 87, no. 11, pp. 113108-113116, 2016.
- [102] W. K. Ridgeway, D. P. Millar and J. R. Williamson, "Vectorized data acquisition and fast triple-correlation integrals for Fluorescence Triple Correlation Spectroscopy.," *Computer Physics Communications*, vol. 184, no. 4, pp. 1322-1332, 2013.
- [103] S. . Kalinin, R. . Kühnemuth, H. . Vardanyan and C. A. Seidel, "Note: A 4 ns hardware photon correlator based on a general-purpose field-programmable gate array development board implemented in a compact setup for fluorescence correlation spectroscopy," *Review of Scientific Instruments*, vol. 83, no. 9, p. 096105, 2012.
- [104] J. . Buchholz, J. . Krieger, G. . Mocsár, B. . Kreith, E. . Charbon, G. . Vámosi, U. . Kebschull and J. . Langowski, "FPGA implementation of a 32x32 autocorrelator array for analysis of fast image series," *Optics Express*, vol. 20, no. 16, pp. 17767-17782, 2012.
- [105] T. A. Laurence, S. . Fore and T. . Huser, "A fast, flexible algorithm for calculating correlations in Fluorescence Correlation Spectroscopy," *Optics Letters*, vol. 31, no.

- 6, p., 2005.
- [106] D. Magatti and F. Ferri, "25 ns software correlator for photon and fluorescence correlation spectroscopy," *Review of Scientific Instruments*, vol. 74, no. 2, pp. 1135-1144, 2003.
- [107] R. A. Colyer, G. Scalia, I. Rech, A. Gulinatti, M. Ghioni, S. Cova, S. Weiss and X. Michalet, "High-throughput FCS using an LCOS spatial light modulator and an 8 x 1 SPAD array," *Biomedical Optics Express*, vol. 1, no. 5, pp. 1408-1431, 2010.
- [108] M. Wahl, I. Gregor, M. Patting and J. Enderlein, "Fast calculation of fluorescence correlation data with asynchronous time-correlated single-photon counting," *Optics Express*, pp. 3583-3591, 2003.
- [109] E. Schaub, "F2Cor: fast 2-stage correlation algorithm for FCS and DLS," *Optics Express*, pp. 2184-2195, 2012.
- [110] E. Schuab, "High countrate real-time FCS using F2Cor," *Optics Express*, pp. 23543-23555, 2013.
- [111] "Virtex-5 Family Overview," 21 August 2015. [Online]. Available: https://www.xilinx.com/support/documentation/data_sheets/ds100.pdf. [Accessed 21 March 2019].
- [112] S. T. Hess and W. W. Webb, "Focal volume optics and experimental artifacts in confocal fluorescence correlation spectroscopy.," *Biophysical Journal*, vol. 83, no. 4, pp. 2300-2317, 2002.
- [113] E. Schaub, High countrate real-time FCS using F2Cor, Optical Society of America, 2013.
- [114] W. K. Ridgeway, D. P. Millar and J. R. Williamson, "Fluorescence Triple Correlation Spectroscopy Resolves Ten Intermediates Along Different Parallel Ribosome Assembly Pathways," *Biophysical Journal*, vol. 102, no. 3, pp. 5-9, 2012.
- [115] D. E. Koppel, "Statistical accuracy in fluorescence correlation spectroscopy," *Physical Review*, pp. 1938-1945, 1974.
- [116] M. Shimizu, S. Sasaki and M. Tsuruoka, "DNA Length Evaluation Using Cyanine Dye and Fluorescence Correlation Spectroscopy," *Biomacromolecules*, vol. 6, pp. 2703-2707, 2005.
- [117] J. W. Krieger and J. Langowski, "QuickFit 3.0 (compiled: 2015-10-29, SVN: 4465): A data evaluation application for biophysics," 2010-2019. [Online].

- Available: http://www.dkfz.de/Macromo/quickfit/. [Accessed 21 06 2019].
- [118] D. E. Koppel, "Study of Escherichia coli Ribosome by Intensity Fluctuation Spectroscopy of Scattered Lase Light," *Biochemistry*, pp. 2712-19, 1974.
- [119] R. Gabler, E. W. Westhead and N. C. Ford, "Studies of Ribosomal Diffusion Coefficients using laser light-scattering spectroscopy," *Biophysical Journal*, pp. 528-545, 1974.
- [120] C. Joo, H. Balci, Y. Ishitsuka, C. Buranachai and T. Ha, "Advances in Single-Molecule Fluorescence Methods for Molecular Biology," *Annual Review Biochemistry*, pp. 51-76, 2008.
- [121] C. . Chen, B. H. Stevens, J. . Kaur, D. . Cabral, H. . Liu, Y. . Wang, Y. . Wang, H. . Zhang, G. . Rosenblum, Z. . Smilansky, Y. E. Goldman and B. S. Cooperman, "Single-Molecule Fluorescence Measurements of Ribosomal Translocation Dynamics," *Molecular Cell*, vol. 42, no. 3, pp. 367-377, 2011.
- [122] Y. Wang, H. Qin, R. D. Kudaravalli, S. V. Kirillov, G. T. Dempsey, D. Pan, B. S. Cooperman and Y. E. Goldman, "Single-Molecule Structural Dynamics of EF-G-Ribosome Interaction during Translocation†," *Biochemistry*, vol. 46, no. 38, pp. 10767-10775, 2007.
- [123] M. E. Altuntop, C. T. Ly and Y. . Wang, "Single-Molecule Study of Ribosome Hierarchic Dynamics at the Peptidyl Transferase Center," *Biophysical Journal*, vol. 99, no. 9, pp. 3002-3009, 2010.
- [124] T. M. Hansen, S. N. S. Reihani, L. B. Oddershede and M. A. Sørensen, "Correlation between mechanical strength of messenger RNA pseudoknots and ribosomal frameshifting," *Proceedings of the National Academy of Sciences of the United States of America*, vol. 104, no. 14, pp. 5830-5835, 2007.
- [125] P. Schwille and E. Haustein, "Fluorescence Correation Spectroscopy: Novel Variations of an Established Technique," *Annu. Rev. Biophys. Biomol. Struct.*, pp. 151-169, 2007.
- [126] E. Gratton and M. A. Digman, "Lessons in Fluctuation Correlation Spectroscopy," *Annu. Rev. Phys Chem.*, pp. 645-668, 2011.
- [127] M. S. Capel, M. Kjeldgaard, D. M. Engelman and P. B. Moore, "Positions of S2, S13, S16, S17, S19 and S21 in the 30 S Ribosomal Subunit of Escherichia coli," *J. Mol. Biol.*, pp. 65-87, 1987.
- [128] Z. . Shajani, M. T. Sykes and J. R. Williamson, "Assembly of Bacterial Ribosomes," *Annual Review of Biochemistry*, vol. 80, no. 1, pp. 501-526, 2011.

- [129] M. Nomura and W. A. Held, "Reconstitution of Ribosomes: Studies of Ribosome Structure, Function and Assembly," *Cold Spring Harbor Monograph Archive*, vol. 04, no., pp. 193-223, 1974.
- [130] R. Chulluncuy, C. Espiche, J. A. Nakamoto, A. Fabbretti and P. Milon, "Conformational Response of 30S-bound IF3 to A-Site Binders Streptomycin and Kanamycin," *The Journal of Antibiotics*, vol. 5, no. 4, p. 38, 2016.
- [131] J. D. Puglisi, A. Petrov and C. E. Aitken, "Single Ribosome Dynamics and the Mechanism of Translation," *Annual Review of Biophysics*, pp. 491-513, 2010.
- [132] J. B. Munro, R. B. Altman, C.-S. Tung, J. H. D. Cate, K. Y. Sanbonmatsu and S. C. Blanchard, "Spontaneous formation of the unlocked state of the ribosome is a multistep process," *Proceedings of the National Academy of Sciences of the United States of America*, vol. 107, no. 2, pp. 709-714, 2009.
- [133] L. S. R. K. J. C. H. T. H. S. Lee J, "Single-molecule four-color FRET," *Angew Chem Int Ed Engl.*, pp. 9922-9925, 2010.
- [134] C. J. a. T. H. Sungchul Hohng, "Single-Molecule Three-Color FRET," *Biophysical Journal*, pp. 1328-1337, 2004.
- [135] J. A. Dunkle and J. H. D. Cate, "Ribosome Structure and Dynamics During Translocation and Termination," *Annual review of biophysics*, vol. 39, no. 1, pp. 227-244, 2010.
- [136] D. G. Knyazev, A. Lents, E. Krause, N. Ollinger, C. Siligan, D. Papinski, L. Winter, A. Horner and P. Pohl, "The Bacterial Translocon SecYEG Opens upon Ribosome Binding," *The Journal of Biological Chemistry*, pp. 17941-17946, 2013.
- [137] A. Kedrov, I. Kusters, V. V. Krasnikov and A. J. Driessen, "A single copy of SecYEG is sufficient for preprotein translocation," *The EMBO Journal*, pp. 4387-4397, 2011.
- [138] I. . Taufik, A. . Kedrov, M. . Exterkate and A. J. M. Driessen, "Monitoring the Activity of Single Translocons," *Journal of Molecular Biology*, vol. 425, no. 22, pp. 4145-4153, 2013.
- [139] Z. C. Wu, J. d. Keyzer, A. Kedrov and A. J. Driessen, "Competitive Binding of the SecA ATPas and Ribosomes to the SecYEG Translocon," *The Journal of Biological Chemistry*, pp. 7885-7895, 2012.
- [140] D. N. Ermolenko, P. C. Spiegel, Z. K. Majumdar, R. P. Hickerson, R. M. Clegg and H. F. Noller, "The antibiotic viomycin traps the ribosome in an intermediate state of translocation," *Nature Structural & Molecular Biology*, pp. 493-497, 2007.

- [141] C. T. Ly, M. E. Altuntop and Y. Wang, "Single-Molecule Study of Viomycin's Inhibition Mechanism on Ribosome Translocation†," *Biochemistry*, pp. 9732-9738, 2010.
- [142] E. L. Elson and D. . Magde, "Fluorescence correlation spectroscopy. I. Conceptual basis and theory," *Biopolymers*, vol. 13, no. 1, pp. 1-27, 1974.
- [143] S. . Maiti, U. . Haupts and W. W. Webb, "FLUORESCENCE CORRELATION SPECTROSCOPY: DIAGNOSTICS FOR SPARSE MOLECULES," *Proceedings of the National Academy of Sciences of the United States of America*, vol. 94, no. 22, pp. 11753-11757, 1997.
- [144] P. Schwille and E. P. Petrov, "State of the Art and Novel Trends in Fluorescence Correlation Spectroscopy," *Standardization and Quality Assurance in Fluorescence Measurements*, pp. 145-197, 2008.
- [149] L. Yang, H. Lee, M. Wang, X. Lin, K. Hsu, Y. Chang, Q. Fann and J. White, "Real-time data acquisition incoropating high-speed software correlator for single-molecule spectroscopy," *J. Microsc.*, pp. 302-10, 2009.
- [150] P. Moore, "How Should We Think About the Ribosome?," *Annual Review of Biophysics*, vol. 41, pp. 1-19, 2012.

VITA

Zenia Norman was born in Grambling, Louisiana. She attended Grambling State
University, where she double-majored in Electronics Engineering Technology and
Drafting Design Technology. Upon graduating, she was accepted into the University of
Missouri and the National Science Foundation's Integrated Graduate Research
Traineeship (IGERT) program. Her research involves building optical instruments and
programming software to investigate the characteristics of biological molecules using
fluorescent techniques.